CZECH TECHNICAL UNIVERSITY
IN PRAGUE

Faculty of Nuclear Sciences and Physical
Engineering

Department of Physics

Bachelor thesis

Transverse flow anisotropies in ultrarelativistic nuclear collisions

Renata Kopečná

Supervisor: doc. Mgr. Boris Tomášik, Ph.D.

Prague, 2014

ČESKÉ VYSOKÉ UČENÍ TECHNICKÉ
V PRAZE
Fakulta Jaderná a Fyzikálně Inženýrská
Katedra Fyziky

Bakalářská práce

Anizotropie příčného toku v ultrarelativistických jaderných srážkách

Renata Kopečná

Supervisor: doc. Mgr. Boris Tomášik, Ph.D.

Praha, 2014

NASCANOVAT PODEPSANE ZADANI A
ULOZIT DO DVOU EPS SOUBORU
ZADANI1.EPS a ZADANI2.EPS

NASCANOVAT PODEPSANE ZADANI A
ULOZIT DO DVOU EPS SOUBORU
ZADANI1.EPS a ZADANI2.EPS

Prohlášení:

Prohlašuji, že jsem svou bakalářskou práci vypracovala samostatně a použila jsem pouze podklady (literaturu, projekty, software, atd.) uvedené v přiloženém seznamu.

Nemám závažný důvod proti užití tohoto školního díla ve smyslu § 60 Zákona č. 121/2000 Sb., o právu autorském, o právech souvisejících s právem autorským a o změně některých zákonů (autorský zákon).

V Praze dne

Renata Kopečná

Title:

Transverse flow anisotropies in ultrarelativistic nuclear collisions

Author: Renata Kopečná

Specialization: Experimental nuclear physics

Sort of project: Bachelor thesis

Supervisor: doc. Mgr. Boris Tomášik, Ph.D.

Abstract:

The quark-gluon plasma (QGP) is a newly-discovered form of matter, where quarks and gluons are asymptotically free. Although it was predicted to behave as a gas, its behavior meets the requirements of almost perfect fluid behavior. Our goal is to study its properties via so-called *anisotropic flow*.

QGP is produced in high-energy nuclear collisions, observed in facilities such as Relativistic Heavy Ion-Collider (RHIC) or Large Hadron Collider (LHC). This form of deconfined matter is very similar to the matter produced in the first microseconds after the Big Bang.

The flow anisotropy reflects the initial energy density fluctuations, due to the low shear viscosity, leading to better knowledge of the initial state of collision. Furthermore, it can help us better understand the evolution of the collision.

The aim of this thesis is to introduce collective flow, its anisotropies and methods used to estimate the flow. Moreover, we study its properties via mathematical models and present our work with Monte Carlo model DRAGON.

Key words: Quark-Gluon plasma, heavy-ion collisions, transverse flow anisotropies, elliptic flow, DRAGON

Název práce:

Anizotropie příčného toku v ultrarelativistických jaderných srážkách

Autor: Renata Kopečná

Abstrakt:

Kvark-gluonové plazma (QGP) je nedávno objevená forma hmoty, v níž jsou kvarky a gluony asymptoticky volné. Původně se předpokládalo, že se QGP bude chovat jako plyn, nicméně výsledky naznačují, že QGP je kapalinou. Naším cílem je zkoumat vlastnosti tohoto plazmatu pomocí anizotropií toku.

QGP je produkováno při vysokoenergetických jádro-jaderných srážkách. Tyto srážky jsou pozorovány ve vědeckých zařízeních jako je relativistický těžko-iontový collider RHIC nebo velký hadronový urychlovač LHC. Tato forma hmoty je velmi podobná té, která byla přítomná v prvních mikrosekunách po Velkém Třesku.

Analýza toku může díky malé smykové viskozitě QGP napovědět mnohé o původních fluktuacích hustoty energie, což vede k hlubším znalostem původních podmínek. Stejně tak pomocí toku můžeme zkoumat i vývoj samotné srážky.

Cílem této práce je popsat kolektivní tok, jeho anizotropie a metody, jimiž se kolektivní tok zkoumá. Dále jej studujeme pomocí Monte Carlo modelu DRAGON, jehož výsledky prezentujeme v závěru práce.

Klíčová slova: Kvark-gluonové plazma, těžko-iontové srážky, anizotropie příčného toku, eliptický tok, DRAGON

Acknowledgement

I would like to express my special appreciation to my supervisor, doc. Tomášik. Without his patience, encouragement, questioning my statements and constant help both with physics and programming this thesis would not have been possible. I am also very grateful for his language check. I would also like to thank all the academic staff at the department of physics for their enthusiasm and willingness to help anytime. Besides the academic staff, my sincere thanks goes to fellow classmates for their personal and academic support. Last but not least, special thanks goes to my friends and familly, especially my sister.

Contents

List of Figures

Introduction

High-energy heavy ion collisions provide a unique tool to investigate many topics of present physics. We can study the equation of state of nuclear matter, properties of quark-gluon plasma or its transition back to hadrons. We speak about *ultrarelativistic* particles, meaning their speed is almost the speed of light, leaving their Lorentz factor $\gamma \gg 1$. This means the velocity bigger than $0.95c$. Heavy ions are nuclei much heavier than proton or neutron.

Flow in heavy ion collision is a collective motion of the system. It can be described by the correlation between the space and momentum in the particle production. We usually distinguish *longitudinal flow* and *transverse flow*. Longitudinal flow is fluid motion in the direction of the beam axis, while transverse flow is the motion transverse to the beam axis. Transverse flow evinces azimuthal anisotropies. Its axially symmetric part is called *radial flow*. The anisotropies are a powerful tool to investigate the properties of quark-gluon plasma, since they are caused by the anisotropies in the initial conditions, which propagate in the medium.

In the first part we introduce basic facts about **quark-gluon plasma** and hydrodynamic basics, where we focus on its impact on theory of quark-gluon plasma. We describe the process of transformation from quark-gluon plasma to free-streaming hadrons. Also, we discuss experimental evidence of the existence of quark-gluon plasma.

The second section describes **collective flow**, its properties and measurements, done at experimental devices RHIC and LHC, comparing them to theoretical calculations. We focus on elliptic flow and its relation to higher-order differential flows.

In chapter **Measurements** we discuss difficulties we have to deal with while measuring collective flow and its anisotropies. Several methods for the determination of collective flow are described and compared. Also, we discuss the contribution to flow that does not originate in initial anisotropies in the energy distribution. For illustration, we present several results obtained mainly at the LHC.

Last chapter introduces our work on a **toy model**. Our task was to construct a toy model

of a profile of the azimuthal angle distribution by using a Monte Carlo algorithm to produce pions with certain transverse momentum. Next step was to compute the n^{th} differential flows using correlations and histogram. In this section, we describe production of non-uniform distribution using random number generators with uniform distribution. Next, the model DRAGON [1] is introduced and it is used as a source of data for our n^{th} differential flows analysis.

1 Introduction to quark-gluon plasma

First predictions of quark-gluon plasma (QGP) appeared in the 1970's. The existence of ultra-dense matter with deconfined quarks and gluons (this means that they are free to move over distances larger than size of a hadron) was predicted owing to the theory of asymptotic freedom, formulated in 1973 by David Gross, Frank Wilczek and David Politzer. *Exploring new phenomena by distributing high energy or high nuclear matter density over a relatively large volume* [2] was first discussed at Bear Mountain workshop in 1974 by T. D. Lee and G. C. Wick [3].

The idea of using heavy-ion collision to explore this new state of matter, named *Quark-gluon plasma* by E. Shuryak, appeared first in 1980 at the workshop "Statistical Mechanics of Quraks and Gluons" in the Center for Interdisciplinary Research at Bielefeld University, Germany. Later, the improvement of relativistic hydrodynamic theory made it possible to investigate the QGP further [3].

1.1 Quark-gluon plasma

Quark-gluon plasma (QGP) is very dense state of matter expected to be present few microseconds after the Big Bang. Nowadays, it is present in the first fm/c during high-energy heavy-ion collisions. Due to the analogy with the expansion of hot universe, these collisions are called *Little Bangs*.

The name *plasma* comes from the similarity with classic plasma, where neutral atoms are changed into ions and free electrons. In QGP, the energy density is extremely high, hadrons are so close to each other that they are dissolved into deconfined colored degrees of freedom, quarks and gluons, carrying color charge - red, green and blue. Chiral symmetry is restored.

QGP comes into existence when the temperature is high enough, reaching *critical temperature* T_c, depending on baryon chemical potential. It is illustrated in fig. 1, the critical temperature is denoted by the green hatching. Black lines are denoted in the picture, they represent chemical and thermal freeze-out. The arrow from the SPS chemical freeze-out to

thermal freeze-out indicates isentropic expansion. However, there is a discussion about the value of T_c even for zero chemical potential. Lattice calculations indicate a value about 160 MeV, however, it differs from paper to paper.

RHIC measurements of quark-gluon plasma quantitatively agree with almost perfect fluid hydrodynamics. This leads to the ascertainment that QGP is a strongly coupled liquid system [5]. One of the most significant properties is its low shear viscosity η/s, where s is the entropy density. At lower limit, its value appears to be approximately $\hbar/4\pi$ [5]. This property allows us to study the QGP phase from the anisotropic flow: the low viscosity implies small energy dissipation, leading to the possibility of studying the original energy distribution.

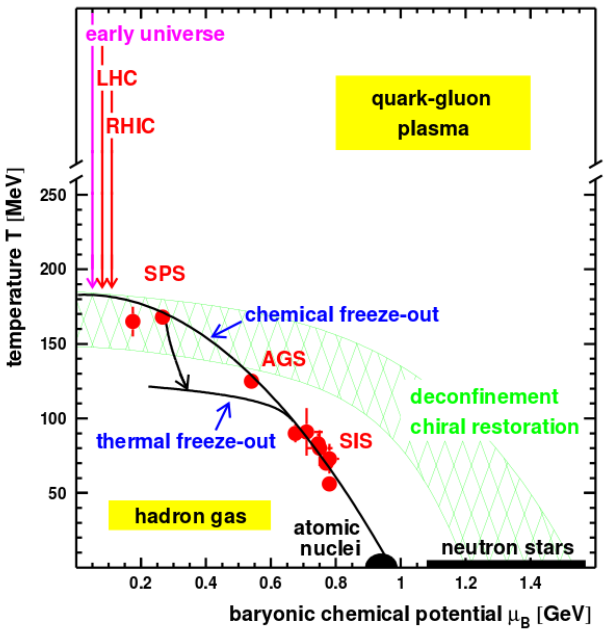

Figure 1: QGP phase diagram, depending on temperature T and baryon chemical potential μ_B. Taken from [4].

Low viscosity is not an extraordinary property. Experiments with very cold liquid helium (temperature below 4.2 K for ^{4}He) evince zero viscosity. However, the entropy density s is also zero [6], so the ratio η/s is not defined. This property of QGP and its consequences are discussed more in section 1.1.2.

This dense matter, produced in Little Bangs, is expanding and cooling down, allowing the formation of hadrons. The transition from QGP to a hadronic gas is called hadronization. This late hadronic state, after the quarks and gluons are combined back into hadrons, behaves more like a gas and needs to be described by transport simulation [5].

Transport simulation is, as the name suggests, a simulation using the transport theory. Transport theory studies the exchange of mass, momentum and energy. It uses tools from

mechanics, electromagnetism, hydrodynamics or thermodynamics. It agrees well with experimental data for non-equilibrium situations, finite size effects of non-homogeneous N-body phase space and for collective dynamics [7].

1.1.1 Hydrodynamics

Hydrodynamics can be successfully used for the description of the initial QGP phase when the matter is deconfined. The fireball acts like a small drop of hot liquid. Now we will briefly present several pieces of knowledge regarding hydrodynamics. Most of it can be found in any textbook concerning fluid mechanics, our main source is [8].

Every non-perfect liquid has viscosity. In this case, there are two types: *bulk* ζ and *shear* η viscosity. Shear viscosity acts against shearing flows. One can imagine it by putting the liquid between two plates, moving in opposite directions. For more viscous liquids, the force needed to move those plates is bigger than for less-viscous liquids, for non-viscous liquids, no force is needed. For example, this viscosity is bigger for oil than for water. In addition to that a fluid can evince internal friction while expanded or compressed. This property is expressed by bulk viscosity. It is related to the 'compressibility' of the fluid. In a simplified way, bulk pressure acts against the expansion (i.e. for expanding fluid it is negative), while shear pressure acts against flow anisotropies - it tends to erase differences in expansion rates [5]. Main characteristic of perfect fluid is zero shear and bulk viscosity.

We will assume some fluid with density $\rho = \rho(x, y, z, t)$, pressure $p = p(x, y, z, t)$ and the velocity distribution $\vec{v} = \vec{v}(x, y, z, t)$, which fully determine the fluid. The coordinates x,y,z and t refers to a point in space-time, not to a particle in the fluid!

1.1.1.1 Ideal fluid

First, we consider ideal non-relativistic fluid. This means there is neither shear nor bulk viscosity. Several equations are valid:

Equation of continuity:

$$\frac{\partial \rho}{\partial t} + \rho \nabla \vec{v} + \vec{v} \cdot \nabla \rho = 0 \tag{1}$$

The equation of continuity basically says that the 'amount' of fluid entering the system is equal to that leaving the system. We define *mass flux density* $\vec{j} = \rho\vec{v}$, representing the mass of fluid flowing through an area perpendicular to $\vec{v}$.

Euler equation:

$$\frac{\partial\vec{v}}{\partial t} + (\vec{v}\cdot\nabla)\vec{v} = -\frac{1}{\rho}\nabla p \tag{2}$$

This equation originates from the properties of a non-compressible fluid. It represents motion of a fluid caused by the pressure gradient. Since in ideal fluids thermal conductivity vanishes; $ds/dt = 0$, where s is entropy over mass, we get an 'entropy equation of continuity':

$$\frac{\partial(\rho s)}{\partial t} + \nabla(\rho s\vec{v}) = 0\,. \tag{3}$$

We call $\rho s\vec{v}$ the *entropy flux density*[1]. Motion described by the eq. (3) is called *isentropic*. For these fluids, the velocity circulation around a closed contour is constant in time.

For $\vec{v} = \vec{v}(x, y, z, t) = const.$, using Euler's equation, relation $dU = TdS - pdV + \mu dn$ and the definition of enthalpy:

$$H = U + pV \Rightarrow dH = TdS + Vdp + \mu dn \tag{4}$$

we obtain Bernoulli's equation:

$$\frac{v^2}{2} + w = const.\,, \tag{5}$$

where w denotes enthalpy per unit mass.

Furthermore, we define *energy flux density* as $\rho\vec{v}(\frac{v^2}{2} + w)$ and *momentum flux density* tensor as $\Pi_{ik} = p\delta_{ik} + \rho v_\mu v_k$. These quantities represent the energy and momentum arrangement in fluid.

[1] In the case of relativistic fluid, s usually denotes entropy density.

1.1.1.2 Viscous fluid

For viscous fluid, we need to add the shear and bulk viscosity 'factors' η and ζ to the equations above. The momentum flux density acquires the form:

$$\Pi_{ik} = p\delta_{ik} + \rho v_i v_k - \sigma'_{ik} = -\sigma_{ik} + \rho v_i v_k \,. \tag{6}$$

The term σ'_{ik} is called *viscous stress tensor* and can be expressed by the equation

$$\sigma'_{ik} = \eta \left(\frac{\partial v_i}{\partial x_k} + \frac{\partial v_k}{\partial x_i} - \delta_{ik} \frac{3}{2} \frac{\partial v_l}{\partial x_l} \right) + \zeta \delta_{ik} \frac{\partial v_l}{\partial x_l} \,. \tag{7}$$

The physical reason for this equation is following; the shear viscosity contributes to the fluid motion only when there is a force causing the friction, hence the first term. From the definition of momentum flux density for perfect fluids it is obvious that for $\vec{v} = \text{const}$, $\sigma'_{ik} = 0$, σ'_{ik} depends on velocity derivation in all terms. Moreover, there is no friction in the case of rotating fluid with constant angular velocity: the term $\partial v_i/\partial x_k + \partial v_k/\partial x_i$ vanishes.

Navier-Stokes equation: This equation describes the motion of non-ideal fluids. In an inertial frame of reference, the equation is:

$$\rho \left(\frac{\partial \vec{v}}{\partial t} + \vec{v} \cdot \nabla \vec{v} \right) = -\nabla p + \eta \Delta \vec{v} + \left(\zeta + \frac{\eta}{3} \right) \nabla \left(\nabla \cdot \vec{v} \right) + \vec{f} , \tag{8}$$

$\vec{f}$ represents forces affecting the fluid (e.g. gravity or electrical field). We assume that the shear and bulk viscosities are constant through the fluid. Worth mentioning is the fact that for incompressible fluid we obtain $\nabla \vec{v} = 0$.

All the equations above are applicable only for the non-relativistic fluids. Some modifications are required in order to express these terms in the relativistic case.

1.1.1.3 Relativistic fluid

For simplicity, we will focus on ideal fluid. First, we need to write down the energy-momentum four-tensor for the fluid in motion. In local rest frame, where the fluid is at rest and Pascal

law is true (pressure is the same in all directions and it is perpendicular to the fluid's surface), we obtain:

$$T^{\mu\nu} = \begin{pmatrix} \epsilon & 0 & 0 & 0 \\ 0 & p & 0 & 0 \\ 0 & 0 & p & 0 \\ 0 & 0 & 0 & p \end{pmatrix} \tag{9}$$

$T^{00} = T_{00}$ is the energy density, denoted as ϵ, $T^{0j}/c = -T_{0j}/c$ is the momentum density, multiplied by c^2 it represents the energy flux density, $T^{ij} = T_{ij}$ is momentum flux density tensor. It is worth reminding that p denotes pressure, not momenta. Transformation of the tensor into some frame of reference is simple; all we need is the fluid's four-velocity $u^\mu = \gamma(1, \vec{v})$:

$$T^{\mu\nu} = wu^\mu u^\nu - pg^{\mu\nu}\,, \tag{10}$$

where w is enthalpy function per volume, g is a metric tensor with $g^{00} = 1$ and $g^{11} = g^{22} = g^{33} = -1$, other components are zero.

The law of conservation of energy and momentum can be expressed as:

$$\frac{\partial T^\nu_\mu}{\partial x^\nu} = 0 \tag{11}$$

Combined with the law of conservation of a quantum number, using flux four-vector $n^\mu = nu^\mu$, we obtain the equation of continuity:

$$\frac{\partial n^\mu}{\partial x^\mu} = 0\,. \tag{12}$$

Worth mentioning is the fact that time component of the flux four-vector is the density and other three components form a 3-D flux vector. This applies only for conserved quantum number, in our case we need to consider formation and annihilation of particles. Moreover, using eq. (10) and considering ideal fluid, we may write

$$\frac{\partial (su^\mu)}{\partial x^\mu} = 0\,, \tag{13}$$

where su^μ represents the entropy flux.

We insert the form (10) into eq. (11) and apply the projector $\Delta^{\mu\nu} = u^\mu u^\nu - g^{\mu\nu}$ on both sides of the equation. The projector $\Delta^{\mu\nu}$ prokects to the direction perpendicular to u^μ. This leasd to the Euler equation:

$$wu^\nu \frac{\partial u_\mu}{\partial x^\nu} = \frac{\partial p}{\partial x^\mu} - u_\mu u^\nu \frac{\partial p}{\partial x^\nu} \tag{14}$$

In case of the isentropic flow, we can obtain Bernoulli's equation:

$$\frac{\gamma w}{n} = const.\,, \tag{15}$$

For viscous thermal-conductive relativistic fluids, we need to re-write the energy-momentum tensor reflecting shear and bulk viscosity $\tau_{\mu\nu} = \tau_{\mu\nu}(\eta, \zeta)$. Moreover, the particle flux density vector has to depend on thermal conductivity κ and chemical potential μ[2] by factor $\nu_\mu = \nu_\mu(\kappa, \mu)$:

$$\begin{aligned} T^{\mu\nu} &= wu^\mu u^\nu - pg^{\mu\nu} + \tau^{\mu\nu}\,, \\ n_\mu &= nu_\mu + \nu_\mu\,. \end{aligned} \tag{16}$$

Even in this case, the conservation of energy-momentum tensor and the equation of continuity are relevant. We define u^μ by the condition that in the proper frame the tensor $T^{\mu\nu}$ acquires the same form as in eq. 10, when no dissipative effects are present

$$\begin{aligned} \tau_{\mu\nu} u^\nu &= 0\,, \\ \nu_\mu u^\mu &= 0 \end{aligned} \tag{17}$$

Using relativistic chemical potential (from eq. (4) $\rightarrow \mu = (w - Ts)/n$) and Gibbs-Duhem equation (19), we obtain entropy flux density:

$$s^\mu = (su^\mu) - \frac{\mu}{T}\nu^\mu\,. \tag{18}$$

[2]Not to be confused with the time-space coordinate.

Gibbs - Duhem equation represents the changes of chemical potential:

$$nd\mu = Vdp - SdT\,. \tag{19}$$

Interesting is the heat conductivity of relativistic fluid. In principle, it is an energy flux without a particle flux. Zero particle flux is expressed as $nu^\alpha + \nu^\alpha = 0$ resulting in energy flux density:

$$cT^{0\alpha} = \frac{cw\nu_\alpha}{n} = \frac{\kappa n T^2}{w^2}\frac{\partial}{\partial x^\alpha}\left(\frac{\mu}{T}\right) \tag{20}$$

For the same reson, the energy flux acquires the form:

$$-\kappa\left(\nabla T - \frac{T}{w}\nabla p\right)\,. \tag{21}$$

This means that the thermal conduction heat flux depends not only on the gradient of temperature, as we may find natural (for non-relativistic case $w \simeq nmc^2$, so the ∇p is omitted), but it also depends on the pressure gradient.

1.1.2 Estimation of shear and bulk QGP viscosity

Despite the success of the description of QGP by perfect-fluid dynamics, the QGP evinces viscosity. It has to be very small, otherwise the perfect-fluid dynamics would not approximately agree with measured data. The question is how small the viscosity is. Estimation of the viscosity is crucial for understanding the event-by-event fluctuations of initial conditions converted into anisotropic flow. This section refers to [5].

As mentioned in the section 1.1, the lower limit for specific shear viscosity η/s is established, using strongly coupled quantum field theories, as $1/(4\pi)$ [5], assuming $c = \hbar = 1$. The reason why we focus on the ratio η/s and not just η is very simple: η/s is dimensionless quantity. For the same reason, we focus on the specific bulk viscosity ζ/s. Moreover, we use *scaled relaxation times* $T\tau_\zeta$ and $T\tau_\eta$ instead of relaxation times τ_ζ, τ_η. Relaxation time is the time required for the system to return to local thermal equilibrium. We also consider

the expansion rate $\theta = \partial_\mu u^\mu$ much smaller than $\tau_{\zeta,\eta}^{-1}$. This requirement guarantees that the fireball is kept in local thermal equilibrium during the expansion.

Assuming small or zero net baryon number, the effects of heat conductivity can be omitted. This assumption works for LHC or RHIC energies.

Small viscosity implies small dissipative effects. This means that initial fluctuations are not erased during the freeze-out stage and survive in the form of anisotropic flow.

Flow is produced due to the pressure gradient $\partial_\mu p$. The crucial function for hydrodynamic evolution is $c_s^2 = c_s^2(\epsilon)$. The relation $\epsilon = \epsilon(T)$ is not necessarily required. However, T depends on microscopic composition and is required for the estimation of final particle production from fireball.

The heat conductivity in QGP is not very explored. Considering leading-order calculations, the obtained viscosity or heat conductivity is too large to result in such a large anisotropic flow. The numerical estimation of η and ζ from QCD (quantum chromo-dynamics) is computationally expensive, so far the results have too large statistical errors.

Very interesting results come from the AdS/CFT correspondence, also called *gauge theory - gravity correspondence*. This theory originates in the string theory and it was first introduced by Juan Maldacena in 1997. The full name is Anti-de-Sitter/Conformal field theory correspondence. It uses the correspondence between five dimensional spaces with quantum gravity and four-dimensional gauge theory using non-Abelian Lie groups [9]. It establishes $\eta/s = (4\pi)^{-1}$ and $\zeta/s = 2/3 - 2c_s^2$. QCD results for η/s are bigger than those obtained from AdS/CFT, while for ζ/s they are smaller.

Combining all the calculations, including heat conductivity, η/s has a minimum near T_c, while ζ/s reaches maximum near T_c.

Another possibility is, of course, to estimate η and ζ from experimental data. As discussed later in section 1.2.3, since the initial energy density in the collision area is not homogeneous, any interaction inside the fireball causes anisotropic flow. When the pre-hydrodynamic stage is connected with the energy-momentum tensor (9), the correlations between particles are transformed into non-vanishing flow anisotropies. Since the viscosity is small, these initial

flow anisotropies survive hydrodynamic stage and the final spectra is strongly dependent on the initial conditions.

Combining with the effect of blue shift (see 1.2.1) the bulk viscosity causes the final p_T spectra to fall more steeply. However, shear viscosity tends to make them flatter. This also means that it is not easy to separate shear and bulk viscosity in measurements.

We could measure shear viscosity by increasing the magnitude of transverse flow while decreasing its anisotropies. This method reflects the shear viscosity present during the whole time of the presence of fireball. The problem is that there is no way to do so. We can also establish it by establishing the deviation δf from the final phase-space distribution $f = f(x,p) = f_0(x,p) + \delta f(x,p)$. This method reflects only the viscosity present in the final hadronization. The disadvantage here is that this approach is reliable only for $p_T \lesssim 2$ GeV. Focusing more on shear viscosity (it affects fireball evolution more than bulk viscosity), smaller δf provides better results.

Final p_T spectra are also affected by the fact that heavier particles' blueshift is bigger than that for light particles. This leads to a flattening of p_T spectra at lower values. It means that any η/s estimation is strongly dependent on the chemical composition at freeze-out used in every model of fireball. To eliminate these effects, the p_T spectrum is compared to *charged hadron* $v_n(p_T)$, where v_n is n^{th} differential flow, discussed in section 2. Illustration of flattened spectra is in fig. 2. The figure depicts p_T spectra from up to 2 GeV for pions (10 centrality bins) and protons (5 centrality bins) produced at Au-Au collisions at $\sqrt{s_{NN}} = 200$ GeV, done by PHENIX and STAR experiments. The data are compared to theoretical calculations of viscous hydrodynamics for 3 different shear viscosities and for ideal fluid. The pion spectra decreas on the momentum interval 2 GeV/c by factor of $\sim 10^4$, while proton spectra decreas by factor of ~ 10. This flattening is more visible at LHC energies than at RHIC energies. However, not all the differences between protons and pions come from flow; many hadrons arise later in decays of unstable resonances, contributing to low p_T. The spectra are also influenced by decoupling temperature; lower decoupling temperature means lower mean transverse momentum. On the other hand, stronger flow means higher $\langle p_T \rangle$, thereby

increasing the apparent temperature.

To sum up, for determination of shear and bulk viscosities both azimuthally averaged transverse momentum spectra and azimuthal anisotropies are needed. For $\eta/s = 0.08$ and $\zeta/s = 0.04$, Glauber model initial condition, predictions agree well with measured data from STAR and PHENIX collaborations.

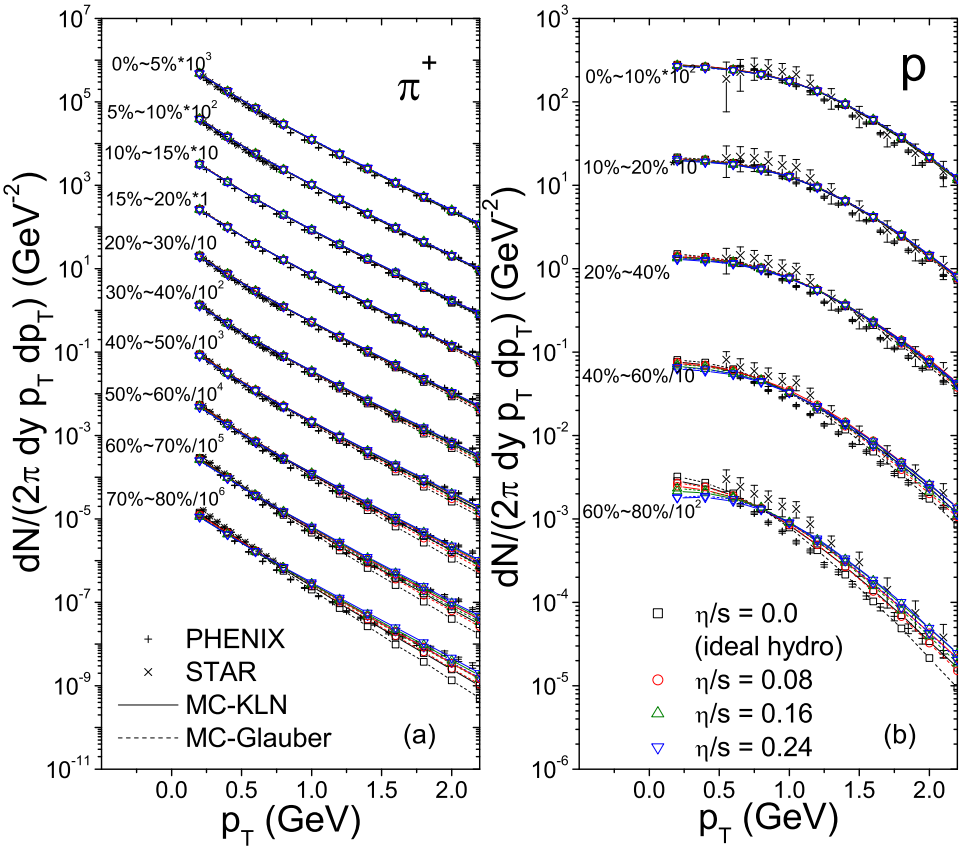

Figure 2: p_T spectra for pions and protons produced at Au-Au collisions at 200 A GeV and its comparison to hydrodynamic prediction. Taken from [5].

1.2 Evolution of the collision

We will assume high-energy heavy-ion collision. During this collision, small drop of very hot and dense matter called *fireball* is created. At the beginning, the QGP is produced. As the temperature decreases, *hadronization* is observed - a phase transition from deconfined to confined matter. Later, there is the *chemical freeze-out* - hadronic chemical equilibrium is no longer maintained. After *chemical freeze-out*, hydrodynamics starts to break down. During all this stages, the drop of matter is called *fireball*. Final step is the *thermal freeze-out* - change from strongly coupled system to a *free-streaming* system. In this section, we discus all the stages in more detail.

Worth mentioning is the pressure gradient. The fireball is produced in vacuum. At the surface of the fireball the pressure is clearly smaller than inside. This pressure gradient $\partial p/\partial \epsilon$ is responsible for generating the flow. The system tends to flow in the direction of the lowest pressure.

1.2.1 Blue shift

As well as we observe red-shift while studying distant bodies, like stars, that are traveling 'from us', blue-shift is present in the case of studying the body traveling 'towards us'. The reason why we observe this phenomenon is very simple: the body emits waves with certain wavelength. As the body is traveling to observer, the wavelength is 'shrinked'. It is the famous Doppler effect: as well as the sound of speeding motorcycle is higher and after passing us it gets deeper, the wavelength of observed particle is shorter as it travels towards the detector. This fact has to be taken into account when counting final p_T spectra. The p_T spectrum is affected by the wavelength, since de Broglie wave's wavelength is $\lambda = h/p$, h is Planck constant.

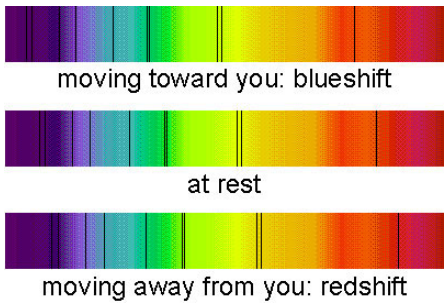

Figure 3: Blue shift illustration. Taken from `http://snap.lbl.gov/science/darkenergy.php`.

1.2.2 Hadronization

Hadronization at the highest RHIC energy and at LHC is a cross-over. There is no precise temperature at which this transition happens, it is rather smooth and fast.[3]

In other words, there is no discontinuity in the energy density as a function of temperature. An example is shown in fig. 4. The figure presents result from lattice QCD simulation. The computation considered various species of quarks, most realistic data is for 2+1 flavours: two light (up and down) and one heavy quark (strange). The contribution from charm quarks is not that significant, as well as from top and bottom, because of their mass. The arrows indicate typical temperatures reached at SPS, RHIC and LHC [10]. It is clear that there is no sharp edge around critical temperature T_c, that would be present in a phase transition. The blue arrow indicates the Stefan Boltzmann limit of the energy density. It corresponds to gas-like behavior of QGP. However, measurements clearly do not match this behaviour, it seems that energy density scaled by T^4 does not increase significantly in the area above 200 MeV.

Hadronization can be also described as a change of the number of degrees of freedom. Under normal conditions, pion gas has 3 degrees of freedom. Above the critical temperature, there are 40 - 50. Since energy density, pressure and entropy are proportional to degrees of freedom, the rapid change in the energy density can be understood as a change of numbers of degrees freedom [10].

1.2.3 Freeze-out

Freeze-out is the transition from interacting system to non-interactiong system. There are two parts of this transition; first, *chemical* freeze-out, followed by *thermal* freeze-out [11]. Af-

[3]Another type of transitions are phase transitions. First-order transitions are transitions, whose first derivatives of Gibbs potential ($G = U + pV - TS$) are discontinuous in the point of transition. Second-order transitions have first derivative continuous, but the second derivatives are discontinuous. Higher order transitions are defined accordingly. Most common are first-order transitions, for example transition from ice to water. During the transition a certain amount of heat is released, proportional to the jump in the discontinuity of the derivative, there is a change of volume. Second-order transition does not evince heat release or change in volume, an example is magnetization in ferromagnetic materials. Higher-order transitions are not observed even though they are theoretically possible.

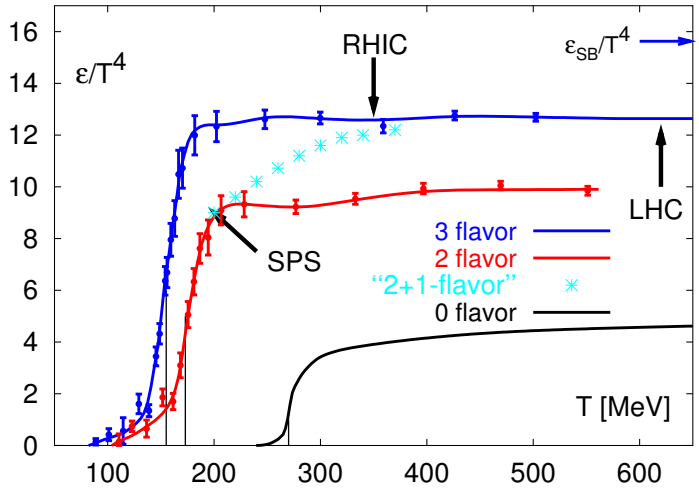

Figure 4: The energy density ε as a function of temperature scaled by T^4 from lattice QCD. Taken from [10].

ter thermal freeze-out, the momenta of particles remain constant, frozen, except for several weak decays. The motivation for studying this phenomenon deeper is simple: hadrons observed after freeze-out carry information about the initial conditions. One can compare it to the microwave-radiation in the early universe: the radiation decoupled much later than nucleosynthesis took place. However, the anisotropies in density distribution, leading to formation of stars and galaxies, can be today observed in the microwave background [11], [12].

1.2.3.1 Chemical Freeze-out

Chemical freeze-out occurs when the inelastic collisions between different species of hadrons become too slow to maintain chemical equilibrium. It occurs *before* the thermal freeze-out. Usually, the cross-section of inelastic collisions is smaller then the cross-section of elastic collisions. As the system cools down, there is not enough energy to maintain inelastic collisions while the elastic ones are still present. Hence, the chemical equilibrium between different hadron species is disrupted, and the final hadron yield is constant. However, the baryon-antibaryon annihilation is still present.

This phenomenon occurs at temperature $T_{chem} \leq T_c$. Below this temperature, in order to keep chemical composition unchanged, it is important to assign different non-equilibrium

chemical potential $\mu = \mu(T)$ to each one of the hadronic species, since the final momentum distribution is affected by them [5].

Since the system is in equilibrium during the chemical freeze-out, we may apply statistical approach [11].

1.2.3.2 Thermal Freeze-out

Simply said, the thermal (or kinetic) freeze-out is a transition from strongly coupled system to free-streaming system. The description of the system by hydrodynamics is no longer possible [5].

This transition is caused by the expansion of the fireball: the expansion is faster than time needed for the particles with mean free path λ_{mfp} to collide with each other. As the density of the fireball decreases, the mean free path of the particles increases. This collision time is denoted τ_{coll} and is determined as following:

$$\tau_{coll} \sim \frac{1}{\sigma n} .$$

The expansion timescale is determined by:

$$\tau_{exp} \sim \frac{1}{\partial_\mu u^\mu} ,$$

where σ is average cross-section, n denotes particle density, u^μ is four-velocity.

It follows that after thermal freeze-out the momentum distribution of particles remains constant. The state when the particles fly freely to detectors is called *free-streaming*.

The condition $\tau_{coll} \geq \tau_{exp}$ implies different thermal freeze-out temperature for particles with different average cross-sections. However, as the expansion is very fast, the kinetic freeze-out is also very fast. Usually, the thermal freeze-out is considered happening at fixed temperature T_f. This condition of constant temperature is very handy, since it defines a three-dimensional hypersurface in Minkowski space [11].

1.2.3.3 Cooper-Fry formula

For the fluid element, the number of particles contained in the volume dV with equilibrium distribution $f_{eq}(E_p)$, E_p denoting energy of the particle, is simply calculated by:

$$dN = dV_\mu \int p^\mu \frac{d^3p}{E_p} f_{eq}(p_\alpha u^\alpha)\,, \tag{22}$$

where the four-velocity u^μ is in the rest frame trivially equal to $(1,0,0,0)$ and where we denote $dV^\mu = dVu^\mu$. The last assumption, however, is not applicable during the freeze-out stage. The reason is connected with the nature of the fireball: particles are emitted just from the surface of the fireball in the space-time. Therefore, for the total particle yield the integration over dV^μ is not applicable. Instead, the hypersurface Σ is used. We get Cooper-Fry formula:

$$N = \int \frac{d^3p}{E_p} \int d\Sigma_\mu(x) p^\mu f(x,p)\,. \tag{23}$$

The calculation of the four-vector $d\Sigma^\mu$ is discussed in detail in [11].

These hypersurfaces are three-dimensional and can be parametrized by coordinates (ϕ,ζ,$\eta_\parallel$):

$$\begin{aligned} t &= [\tau_i + d(\phi,\zeta,\eta_\parallel)\sin\zeta]\cosh\eta_\parallel\,,\\ z &= [\tau_i + d(\phi,\zeta,\eta_\parallel)\sin\zeta]\sinh\eta_\parallel\,,\\ x &= d(\phi,\zeta,\eta_\parallel)\cos\zeta\cos\phi\,,\\ y &= d(\phi,\zeta,\eta_\parallel)\cos\zeta\sin\phi\,. \end{aligned} \tag{24}$$

In these equations, ϕ is the azimuthal angle in the plane x-y, $\eta_\parallel$ is the spacetime rapidity. From the equations we simply get *proper time* τ, initial time for the hydrodynamic stage *initial proper time* τ_i and transverse distance r:

$$\begin{aligned} \tau - \tau_i &= \sqrt{t^2 - z^2} - \tau_i = d(\phi,\zeta,\eta_\parallel)\sin\zeta\,,\\ r &= \sqrt{x^2+y^2} = d(\phi,\zeta,\eta_\parallel)\cos\zeta\,. \end{aligned} \tag{25}$$

The parameter $d(\phi,\zeta,\eta_\parallel)$ is the distance between the hypersurface point $(\phi,\zeta,\eta_\parallel)$ and the

spacetime point ($\tau = \tau_i, x = 0, y = 0$). We focus on this parameter because, usually, the curves of freeze-out are functions of parameter ζ. If d is independent of ϕ, in other words $d = d(\zeta, \eta_\parallel)$, the hypersurface is cylindrically symmetric. Using same argumentation, d independent on $\eta_\parallel$ is boost-invariant. Therefore, we will concentrate on d exclusively dependent on ζ, leaving us with boost-invariant cylindrically symmetric freeze-out hypersurface.

After using the parametrization of rapidity y, transverse mass $m_T = \sqrt{m^2 + p_T^2}$ and four-momenta $p^\mu = (m_T \cosh y, p_T \cos\phi_p, p_T \sin\phi_n, m_T \sinh y)$ we can obtain $d\Sigma_\mu p^\mu$ needed in equation (23) in terms of $d\phi$, $d\zeta$ and $d\eta_\parallel$.

For boost-invariant systems, following the same technique, we obtain six-dimensional particle distribution at freeze-out. For details see [11].

The equation (23) gives the momentum distribution:

$$E_p \frac{dN}{d^3p} = \int d\Sigma_\mu(x) p^\mu f(x,p)\,. \tag{26}$$

Considering particles in local thermodynamic equilibrium, instead of $f(x,p)$ we can use $f_{eq}(p^\alpha u_\alpha)$, since we need the energy in fluid's rest-frame. Thus, the equilibrium distribution function is:

$$f_{eq}(p^\alpha u_\alpha) = \frac{1}{(2\pi)^3}\left[\exp\left(\frac{p^\alpha u_\alpha - \mu}{T}\right) - \delta\right]^{-1}, \tag{27}$$

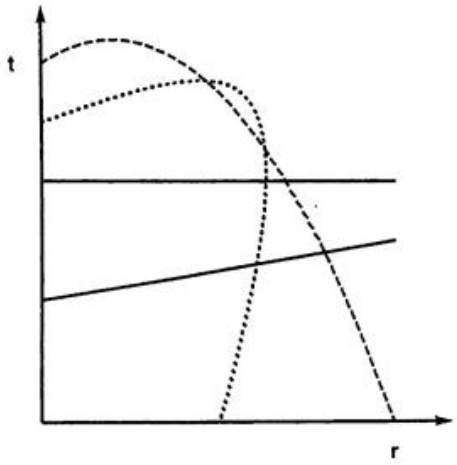

Figure 5: Freeze-out curves in t-r space. Taken from [11].

where $\delta = 1$, -1 or $\delta \to 0$ for Bose-Einstein, Fermi-Dirac or Boltzmann statistics, respectively. This substitution leads to particle distribution:

$$E_p \frac{dN}{d^3p} = \frac{1}{(2\pi)^3}\int d\Sigma_\mu(x) p^\mu \left[\exp\left(\frac{p^\alpha u_\alpha - \mu}{T}\right) - \delta\right]^{-1}. \tag{28}$$

An illustration of the freeze-out hypersurfaces can be seen in fig. 5. Dashed and dotted lines denote curves including both space-like and time-like part, solid lines denote presence of time-like part only.

1.3 Experimental evidence

First data suggesting the existence of QGP were gathered at SPS, CERN [13]. Later, results from all four experiments at RHIC facility, were very auspicious, as well as the newest data from experiments at LHC [10].

Since the detection of such a short time interval as fm/c is impossible, several indirect methods of observation of QGP are used. The main indicator is the transverse flow, in particular *elliptic flow*, discussed in section 2.2, and the quenching of jets.

Partons propagating through dense deconfined medium lose more energy than those traversing confined medium. This leads to a suppression of jets, studied by inclusive spectra and two-particle azimuthal correlation. Convincing results were achieved at STAR experiment at RHIC [14]. Series of measurements of p+p, d+Au and Au+Au collisions at $\sqrt{s_{NN}}$ = 200 GeV, made in the same detector, were analyzed and they suggest formation of a dense deconfined medium.

1.3.1 Nuclear modification factor

Hadron production in d+Au and Au+Au is compared to p+p hadron production via *nuclear modification factor*:

$$R_{AB}(p_T) = \frac{\frac{d^2N}{d\eta dp_T}}{T_{AB}\frac{d^2\sigma^{pp}}{d\eta dp_T}}\,, \tag{29}$$

where AB indicates collision of nuclei A and B, σ^{pp} is the cross-section of p-p collision and T_{AB} is the nuclear overlap function. Nuclear overlap function is defined as

$$T_{AB}(\vec{b}) = \int d^2s T_A(\vec{s}) T_B(\vec{s}-\vec{b})\,, \tag{30}$$

where $\vec{b}$ is impact parameter, T_A is nuclear profile function defined:

$$T_A(\vec{s}) = \int dz \rho_A(\vec{s}, z)\,. \tag{31}$$

$\rho_A(\vec{s}, z)$ denotes nuclear density distribution; the probability of finding a nucleon in a nucleus with the mass A, dependent on z-axis coordinate z and vector $\vec{s}$, connecting the nucleon with the centre of the nuclei. Illustration of vector $\vec{s}_B$ is in the fig. 6. It is displayed in the plane transverse to the z-axis. $\vec{b}$ denotes impact parameter. Practically, the nuclear overlap function T_{AB} stands for the number of binary collisions.

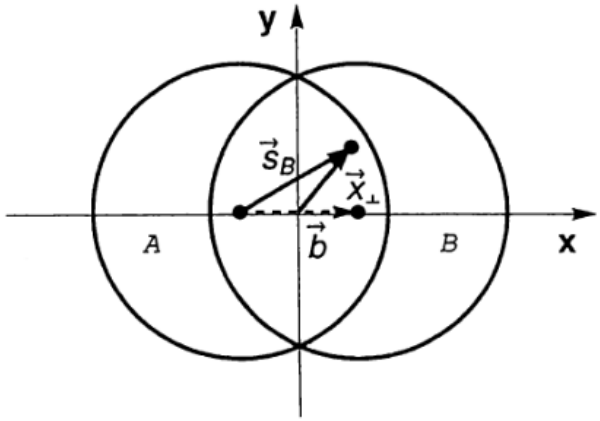

Figure 6: Nucleon-nucleon collision. $\vec{s}_B$ represents the vector between the nucleus center and its nucleon. Taken from [11].

If the nuclei acted as a set of neutrons and protons, colliding without the creation of the dense matter, one would expect the R_{AB} factor for Au-Au collision to be approximately one, because the nucleons would react without significantly affecting each other. $R_{AB} = R_{AB}(p_T)$ for central and minimum-bias d+Au collisions at $\sqrt{s_{NN}} = 200\,\text{GeV}$, presented in fig. 7, reflects the absence of hot and dense medium, whilst the R_{AB} for central Au+Au collisions is highly suppressed and its value is around 0.5. The deviation from one for d+Au collisions is mainly caused by so-called *Cronin effect*. This enhancement of R_{AB} is visible for both d+Au and Au+Au collision in the p_T area around 2 GeV. It is assumed it is caused by multiple scattering effect. Before the particles in the nuceli produce low-p_T particles, they gain p_T from interactions with particles from the other nuclei. This gained p_T is reflected in the final particle spectrum. Furthermore, the Au+Au collisions with larger impact parameter show similar behaviour as p+p and d+Au collisions, indicating that the dense medium is not created in peripheral collisions.

1.3.2 Jet quenching

One of the main indicators of QGP is *jet quenching*. Jet is a collimated hadron shower, produced from high-energy quarks and gluons. Due to color confinement, quarks cannot be observed individually, but always in a quark-antiquark pair (meson) or as a group of three

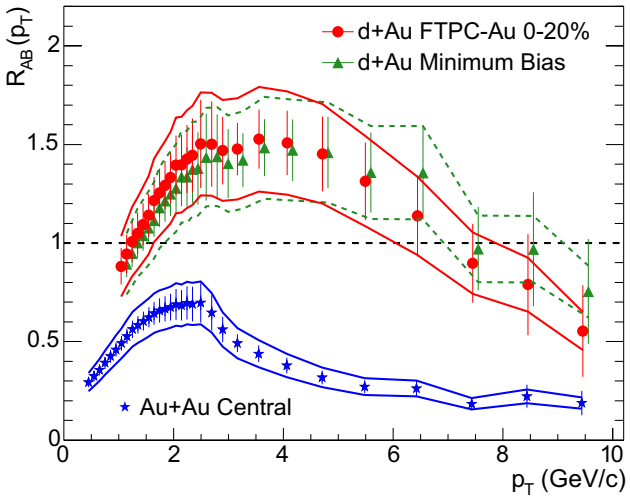

Figure 7: Nuclear modification factor $R_{AB} = R_{AB}(p_T)$ comparison for d+Au and Au+Au collisions at $\sqrt{s_{NN}}$ =200 GeV. The minimum-bias data are shifted 0.1 GeV to the right for better illustration. Error-bars show the normalization uncertainties. Taken from [14].

quarks (baryon)[4]. When quark is hit by another particle hard enough to be separated from hadron, the confinement forces the quark to create mesons or baryons.

Due to the momentum conservation, there are two-jet or three-jet events. The overall jet momentum and the flight direction is the same as the momentum of the leading particle. Two-jet events come from quarks, third jet, if present, originates from a gluon.

Figure 8 shows the comparison of two-particle azimuthal correlation $1/N_{trigger}\frac{dN}{d(\Delta\phi)}$ dependence on $\Delta\phi$ of p+p minimum-bias and central Au+d and Au+Au collision. High p_T triggering was used, meaning that if there was at least one high-p_T hadron, the event was used in the analysis. $N_{trigger}$ is number of such particles. Hence, the quantity $1/N_{trigger}\frac{dN}{d(\Delta\phi)}$ denotes the number of particles normalized by the number of jets.

The data are presented without the pedestal contribution and without the elliptic flow. The peak around $\Delta\phi = 0$ is present for all three kinds of collisions. However, the peak for $\Delta\phi = \pi$ is highly suppressed for central Au+Au collisions. As mentioned before, due to momentum conservation, two jets in opposite directions are produced. The fact that they

[4]Recent measurements indicate the possibility of existence of a *tetraquark*, particle consisting of two quarks and two antiquarks.

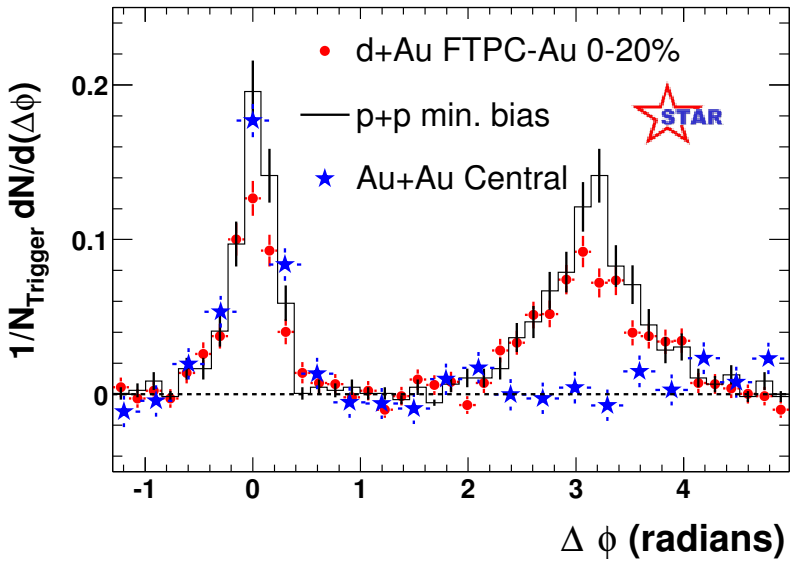

Figure 8: Comparison of two-particle azimuthal correlation for central d+Au collision to p+p and central Au+Au collisions. Taken from [10][5].

are not detected indicates the second jet has to travel through present very dense medium. Considering high p_T particle production suppression in central Au+Au collisions, it follows that QGP is produced in Au+Au and is absent in d+Au collisions.

[5]First appeared in [14], however, this version from [10] is more illustrative.

2 Collective flow

Initial conditions in heavy-ion collisions fluctuate from event to event. It turns out that anisotropies in the *collective flow* are reflected in the particle momentum distribution related to the reaction plane. It can give us information about the initial conditions and about the early evolution of the system, since they are developed mainly in the first moments during the collision [16]. However, the collisions are not symmetric and ideal, there are quantum fluctuations, the initial nuclei geometry varies from event to event, even for fixed impact parameter the initial energy density is anisotropic, QGP is not an ideal fluid. All these effects cause flow anisotropies. Those anisotropies are most significant for non-central collisions. Studying them can provide an insight into QGP properties [17].

Flow is developed during all the stages as discussed in section 1.2. It is a strong evidence of applicability of the almost ideal fluid dynamics. Also, it provides information about the collision evolution and about the initial conditions. As mentioned in the section 1.2, flow is generated by the pressure gradient. It is greater at the surface of the fireball, but there are hotter and colder spots also in the fireball, resulting in stronger anisotropies.

The anisotropies are p_T dependent; for p_T lower than 3 GeV, hydrodynamics is applicable. For intermediate transverse momentum, $p_T \in \langle 3, 6 \rangle$ GeV, flow is smaller for mesons and bigger for baryons. Considering p_T above 8 GeV, the flow is highly dominated by effects caused later in the collision evolution, not by initial conditions anisotropies. The flow is expected to be dominated by high-energy partons. They suffer from big energy loss, caused by radiation and collisions itselves. This loss depends on the thickness of the hot and dense medium they have to transverse. If the system is asymmetric, the energy loss is also asymmetric, leading to azimuthally anisotropic p_T distribution [18].

We study these anisotropies via azumithal distribution of particles. Common approximations is expanding it to Fourier series [11]:

$$\frac{dN}{dyd^2p_T} = \frac{dN}{2\pi p_T dy dp_T}\left[1 + \sum_{n=1}^{\infty} 2v_n \cos(n(\Phi - \Phi_{RP}))\right] . \tag{32}$$

Notation is usual: N is number of particles, p_T indicates transverse momentum, y rapidity, Φ is particle's azimuthal angle relative to the reaction plane, Φ_{RP} is reactions plane azimuthal angle. The reaction plane is theoretically defined as a plane made up by the beam axis and the impact parameter [16]. The v_n coefficients are n^{th} *differential flows*. The average over p_T and y gives us *integrated flow*.

Considering non-central collision, the odd differential flows can be neglected due to symmetry: the matter expansion in the transverse plane has approximately an elliptic shape. Sum over many particles should give these odd coefficients zero.

2.1 Directed flow

The 1^{st} *differential harmonics* represents the deflection of incoming particles in the nuclear collisions. The particles from the overlap region are deflected in opposite directions. This deflection happens very early in the collision. Hence, this quantity is a good probe for the early time of the collision.

Directed flow strongly depends on the collision energy. For lower energies, v_1 linearly rises as a function of rapidity. However, with increasing energy, the directed flow begins to decrease, it even becomes negative. With further increasing of energy, v_1 rises again. The predictions for very high energies suggest it becomes negative once again [16]. There are several possible causes of this phenomenon. Hydrodynamic approach it explains by the QGP phase transition.

Measurements done at RHIC for Au-Au and Cu-Cu collisions evince several interesting characteristics. For illustration, we present directed flow of charged hadrons as a function of pseudorapidity η for centrality bin 30 - 60% in the fig. 9. Solid and dashed curves are polynomial fits. The AMPT calculations are presented only for one side of pseudorapidity for better comprehension. AMPT model is a *multiphase transport model*. The AMPT predicts that directed flow is bigger for heavier particles.

First, the change of sign is not observed. Directed flow simply decreases with increasing pseudo-rapidity. Second, it seems that directed flow is not dependent on colliding nuclei.

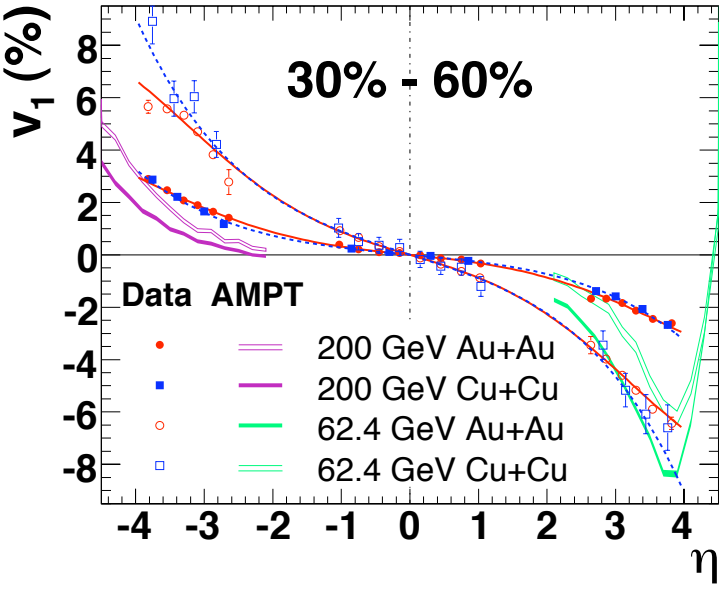

Figure 9: RHIC measurements compared to the AMPT prediction of directed flow. Taken from [16].

Gold is approximately three times heavier than copper. Furthermore, for fixed rapidity, the directed flow decreases with the energy.

2.2 Elliptic flow

The 2^{nd} *differential flow* is called *elliptic flow*. It is considered one of the proofs of QGP existence. If QGP was not produced, particle distribution would be spherical. Elliptic flow originates from several things. First, it is the size of the fireball that depends on the fluctuations of initial state. Part of it emerges from the hadronic phase. These contributions are smaller for higher collision energies. If the collision was totally symmetric and there was no scattering, the elliptic flow should be zero. However, small spatial anisotropies are present. Initial geometry is usually expressed by *eccentricity* ϵ:

$$\epsilon = \frac{\langle y^2 - x^2 \rangle}{\langle y^2 + x^2 \rangle} \,. \tag{33}$$

The brackets represents average taken over some distribution, usually it is energy density. z represents beam direction, x impact parameter and y is perpendicular to both of them. This spatial anisotropy is converted into pressure gradient leading to flow. If eccentricity is small, elliptic flow should be proportional to it, regardless to the chosen weight [16]. However, this approach assumes perfect-fluid properties of QGP and does not reflect all initial anisotropies. Instead, *participant eccentricity* was recently introduced [17]:

$$\epsilon_{part} = \frac{\sqrt{(\langle y^2\rangle - \langle x^2\rangle)^2 + 4\langle xy\rangle^2}}{\langle y^2\rangle + \langle x^2\rangle}\,. \tag{34}$$

Obviously, from the coordinate system, $\langle x\rangle = \langle y\rangle = 0$

At low energies, v_2 can be negative. This is called *squeeze-out* and it is caused by *spectators* - nucleons not participating in the collision. These nucleons shadow the expansion in the plane perpendicular to the beam. At high energies, this phenomenon is not important anymore: relativistic approach becomes applicable. The nuclei are contracted, they gain *pancake* shape - the transverse size of nuclei is much bigger than longitudinal. Moreover, the time needed for the creation of elliptic flow is much bigger than the passing time. Hence, there is not enough space nor time for the spectators to influence the elliptic flow.

For illustration, we present the very first measurements of elliptic flow dependent on the ratio of charged hadron multiplicity to maximum observed multiplicity done at RHIC in fig. 10.

2.3 Higher harmonics

The 3^{rd} *differential flow* is called *triangular flow*. As mentioned above, the main contribution of v_3 are symmetry fluctuations. Moreover, it is not significantly affected by the centrality, proving its origin is in the initial geometry [18]. The 4^{th} *differential flow* is called *quadrangular flow*. Deeper studying of the higher order differential flows began recently at LHC [19]. So far, the focus is mainly on *pentagonal,* v_5, and *hexagonal*, v_6, flows. Due to shear viscosity, anisotropies in the expansion velocity tend to vanish. Therefore, higher harmonics

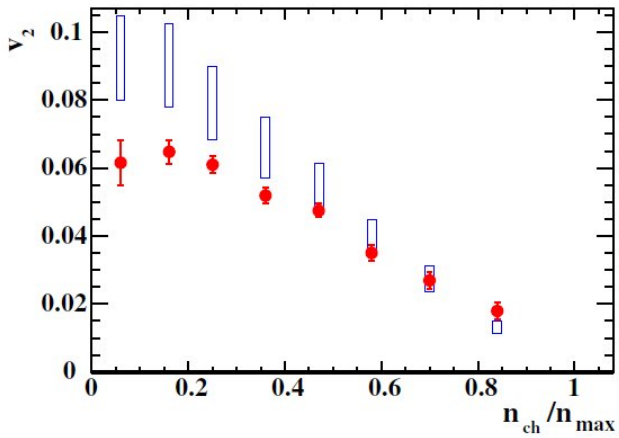

Figure 10: First STAR measurements of elliptic flow. Blue boxes represent hydrodynamic predictions. Taken from [16].

are significantly suppressed with increasing n. It leads to big uncertainties for establishing higher-order harmonics.

Comparison of v_2 - v_6 for eight centrality classes is in the fig. 11. All the flows increase up to 3 GeV then they decrease. The flow is present even in the most central collisions, meaning it is not related only to centrality. All the flows are positive even for the highest p_T (including statistical uncertainties). This phenomenon is connected with the transition of collective anisotropies to jet-path anisotropies.

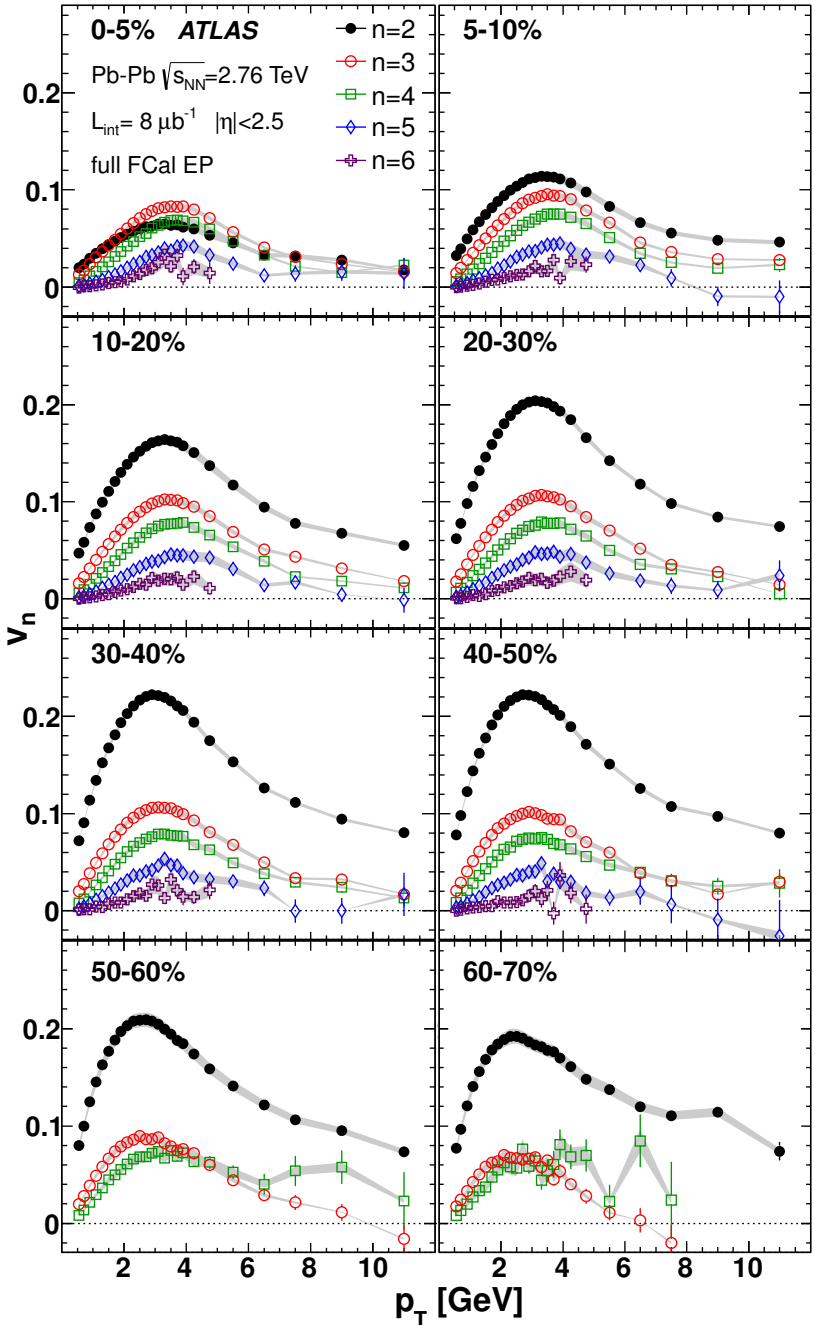

Figure 11: ATLAS $v_2 - v_6$ versus p_T measurements for charged particles produced in Pb-Pb collisions with $\sqrt{s_{NN}} = 2.79$ TeV for eight centrality classes. Shadowed bands denotes systematic uncertainties. Taken from [20].

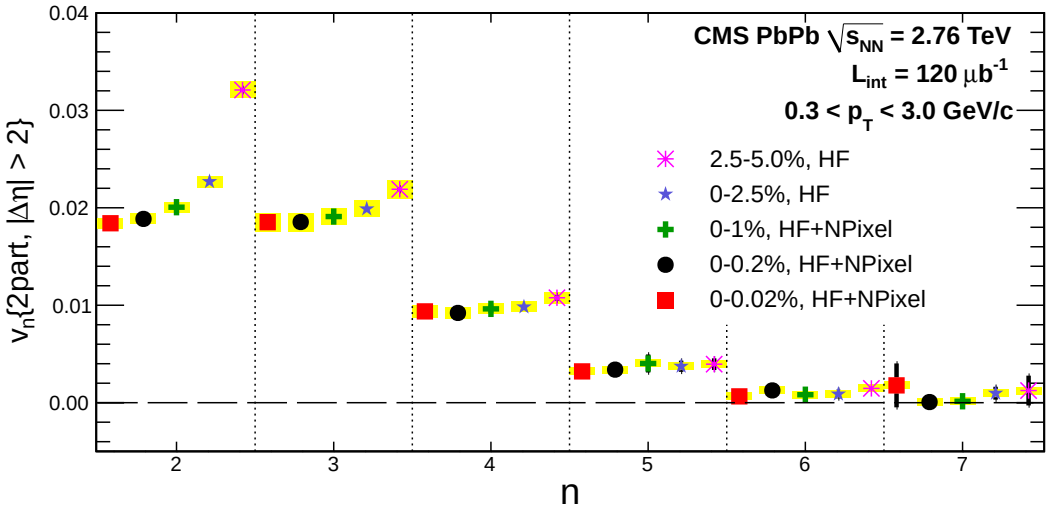

Figure 12: Comparison of p_T-averaged v_n for ultra-central Pb-Pb collisions. Taken from [21].

Very interesting results can be obtained by studying ultra-central collisions. Figure 12 shows results from CMS experiment at LHC for central (centrality up to 5%) and ultra-central Pb-Pb collisions at $\sqrt{s_{NN}} = 2.79$ TeV [21]. In ultra-central collisions, the flow anisotropy caused by the collision non-centrality vanishes. Hence, obtained results are strongly connected with initial state fluctuations. The figure illustrates very strong v_2 and v_3 dependence on centrality. The errors here are denoted by yellow boxes (systematic) and by error-bars (statistical). Interesting fact is that for the most central collisions (0 - 0.2 %) $v_2 \approx v_3$. One would expect that $v_2 > v_3$ due to shear viscosity. This indicates omitting bulk viscosity or higher-order non-linear terms in relativistic transport equation is not a good assumption. However, any theoretical calculation has not successfully reproduced this data yet.

3 Measurements

As mentioned in the previous section when discussing eq. (32), measurements of azimuthal anisotropies in the collective flow is complicated by the fact that it is impossible to establish the impact parameter b. Moreover, the position of nucleons in the nuclei fluctuates event-by-event, so the impact parameter does not provide enough information about initial conditions. In this section, we will discuss mathematical methods used for approximating or substituting the reaction plane, its advantages and disadvantages. Main sources are [16] and [22].

3.1 Computing methods

Even though direct obtaining of reaction plane is impossible, event-by-event analysis of the data can provide us good results. This fact leads to simple conclusion: only rotationally invariant quantities can be measured. Usually, the focus is on two or many particle correlation. This provides the information about the particle relation and makes computation of harmonic flows possible.

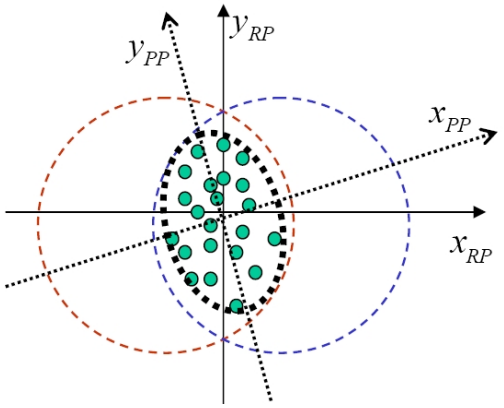

Figure 13: Reaction plane and participant plane definition. Taken from [16].

The reaction plane defined in eq. (32) is measurable only assuming smooth symmetrical matter distribution. For better approximation, symmetry plane Ψ_n is introduced[6]. This plane is determined by participating nucleons, usually being referred to as *participant plane*. It fluctuates event-by-event, due to different initial conditions in every collision. This plane is determined such that sine terms in the Fourier decomposition (eq. (32)) vanish. Graphic illustration can be seen in fig. 13. There is a big difference between obtained $v_n^{(RP)}$ from theory via reaction plane and $v_n^{(PP)}$ obtained via participant plane; for example $v_2^{(PP)} > v_2^{(RP)}$.

[6]Note that Ψ_n is n-dependent, in contrast to eq. (32).

Hence, the obtained v_n is not precisely the n$^{\text{th}}$ coefficient in eq. (32). We define *flow vector* $e^{in\Psi_n}$ and orientation angles Ψ_n

$$v_n e^{in\Psi_n}(p_T,\eta) \equiv \frac{\int_0^{2\pi} d\phi \frac{dN}{d\phi dp_T d\eta} e^{in\phi}}{\int_0^{2\pi} d\phi \frac{dN}{d\phi dp_T d\eta}} \tag{35}$$

and the *average vector flow magnitude* $\overline{v}_n$ together with *average direction* $\overline{\Psi}_n$

$$\overline{v}_n e^{in\overline{\Psi}_n}(p_T,\eta) \equiv \frac{\int_0^{2\pi} d\phi d\eta dp_T \frac{dN}{d\phi dp_T d\eta} e^{in\phi}}{\int_0^{2\pi} d\phi d\eta dp_T \frac{dN}{d\phi dp_T d\eta}} \,. \tag{36}$$

These definitions secure that for a symmetric collision all odd harmonics in Fourier decomposition vanish [17].

Taking into account N particles, the statistical uncertainty is about $\simeq 1/\sqrt{2N}$. Since one-event calculations result in uncertainty even bigger than 50%, many events have to be somehow averaged a weighted [17]. Now, we will present several methods how to do so.

3.1.1 Event plane method

This method uses estimation of the reaction plane - *event plane*. It is defined as the direction of maximum final-state particle density. Because of initial fluctuations, eq. (32) is slightly modified: we introduce event plane angle for every n$^{\text{th}}$ harmonic Ψ_n:

$$\frac{dN}{d\Phi} \propto 1 + \sum_{n=1}^{\infty} 2v_n \cos\left[n(\Phi - \Psi_n)\right], . \tag{37}$$

It is applicable for estimating Ψ_2 - Ψ_6.

First, *event flow vector* $\overrightarrow{Q_n} = (Q_{n,x}, Q_{n,y})$ is defined as

$$\begin{aligned} Q_{n,x} &= \sum_j w_j \cos(n\Phi_j) = |\vec{Q}_n| \cos(n\Psi_n) \,, \\ Q_{n,y} &= \sum_j w_j \sin(n\Phi_j) = |\vec{Q}_n| \sin(n\Psi_n) \,. \end{aligned} \tag{38}$$

The sum goes over all particles, Φ_j denotes lab azimuthal angle. The coefficients w_j are j^{th}'s particle weight, depending on rapidity y. For odd harmonics, $w_i(y) = w_i(-y)$. The coefficients w_j are chosen as an approximation of the n^{th} differential flow. At low transverse momentum, up to 2 GeV, $v_n \sim p_T$. Hence, usual choice for w_j is p_T.

The event plane angle is defined:

$$\Psi_n = \frac{\arctan 2(Q_{n,x}, Q_{n,y})}{n}\,, \tag{39}$$

where arctan2 is two-argument arctan, defined by the equation

$$\varphi = \arctan 2(x, y)\,. \tag{40}$$

Notation is simple; x, y are cartesian coordinates of some 2D vector $\vec{v} = (x, y)$, φ is vector's azimuthal angle in the polar coordinate system.

The n^{th} differential flow is then calculated as an average over all particles for fixed rapidity y and p_T bin and for fixed centrality:

$$v_n^{obs}(p_T, y) = \langle \cos(m(\Phi_j - \Psi_n)) \rangle\,. \tag{41}$$

Here m denotes the *number of correlation*, not harmonic number! If n denotes the harmonic, then $m = kn$, where k is an integer. For $k > 1$ the method is called *mixed harmonics method*, applied usually at fixed-target experiments or to study higher harmonics. Even though this approach is more computationally expensive, it eliminates non-flow effects, discussed later in section 3.2. The number of correlation is handy in the case of measuring e.g. v_4 in the plane Ψ_2. However, the self-correlating components are still present; they can be eliminated by subtracting the $\vec{Q}_{j,n}$ of j^{th} particle from the total $\vec{Q}_n$. Also, since we cannot achieve unlimited number of particles and events, *event plane resolution* is defined as

$$\Re_n = \langle \cos\left[n(\Psi_n - \Psi_{RP})\right] \rangle\,. \tag{42}$$

Angle brackets, again, denote average over all particles for fixed y and p_T. The resolution of the reaction plane is multiplicity-dependent. The final n$^{\text{th}}$ differential harmonics are then obtained by

$$v_n = \frac{v_n^{obs}}{\Re_n} \,. \tag{43}$$

Since in the equation (41) v_n is very centrality-dependent, this equation should be used for narrow centrality bin. Wider centrality class should be divided in narrow bins and then weighted by the bin's multiplicity.

Furthermore, one has to consider the imperfection of detectors. Three methods are used [16]:

- Φ *weighting*: Each particle is weighted with the inverse of the azimuthal distribution of the particles averaged over many events.
- *Recentering*: The average $\vec{Q}$ is subtracted from the $\vec{Q}$ of each event. This implies final zero average $\vec{Q}$. This method is less sensitive to variations in detector's acceptance.
- *Shifting*: The Ψ_n is averaged over many events by Fourier expansion, obtaining the shift for each event plane angle.

3.1.2 Particle correlations

There are several methods to estimate differential flows that use the relation between produced particles. The reason is that the anisotropy in the flow, leading to particle correlation.

3.1.2.1 Pair-wise correlation method

This method is based on the Fourier series expansion of the distribution of pairs in their relative azimuthal angle $\Delta\Phi = \Phi_a - \Phi_b$:

$$\frac{dN^{pairs}}{d\Delta\Phi} \propto 1 + \sum_{n=1}^{\infty} 2v_n^2(p_T^a, p_T^b)\cos(n\Delta\Phi) \,. \tag{44}$$

The correspondent values of v_n^2 are obtained by a fit of the data. Biggest advantage of this method is its simplicity: no event plane is used. However, the obtained harmonic flow is an

integrated flow, which is better to compute as an average of differential flow.

If both of the particles are associated with the same flow anisotropy, we obtain

$$v_n^2(p_T^a, p_T^b) = v_n(p_T^a)v_n(p_T^b)\,. \tag{45}$$

3.1.2.2 Two-particle cumulant method

This method is similar to pair-wise correlation method - instead of two-particle distribution fit, the n$^{\text{th}}$ differential flow is counted directly as

$$v_n\{2\}^2 = \langle\langle\cos\left[n(\phi_i - \phi_j)\right]\rangle_{pair}\rangle = \langle u_{n,i}, u_{n,j}^*\rangle\,. \tag{46}$$

Pair-brackets denote an average over all particle pairs ($i \neq j$). Angular brackets denote an average over all events. The pairs are selected as a particle in a rapidity bin plus unidentified hadron [17], $u_{n,j}$ is j$^{\text{th}}$ particle's *unit flow vector*[7];

$$u_n = e^{in\phi}\,. \tag{47}$$

This method, due to its simplicity, is widely used [22], [20] ,[17] ,[18]. It can be used assuming negligible nonflow, small event plane p_T dependence and mainly approximately constant flow fluctuations. Of course, none of this is true, but in certain situations it is a reasonable approximation. Its difference from v_n is about 10%. If the chosen particles are both from a certain centrality bin, the obtained v_n is an exact result [17].

3.1.2.3 Scalar product method

In contrast to event plane method, this method preserves the information on the length of vector $\overrightarrow{Q_n}$, defined by equation (38). The estimation of n$^{\text{th}}$ differential flow is done according to the following equation:

$$v_n(p_T, y) = \frac{\langle\vec{Q}_n u_{n,j}^*(p_T, y)\rangle}{2\sqrt{\langle Q_n^a Q_n^b\rangle}}\,. \tag{48}$$

[7] Asterisk denotes complex conjugate.

The indexes a and b denote two subevents. Multiplicity is used as a weight. Notice that replacing $\overrightarrow{Q_n}$ by its unit vector reduces this method to the event plane method. The statistical errors are smaller than in the case of event plane method.

3.1.2.4 Multi-particle correlation method

This method uses more than two particle correlations. This method can greatly suppress nonflow effects. Moreover, this method eliminates the acceptance effects. However, there are some disadvantages. The statistical errors are bigger. Sometimes, the square of n^{th} differential flow can be negative, depending on flow fluctuations. Good example can be four-particle correlation, while using two-particle correlation to eliminate two-particle non-flow effect:

$$\langle\langle u_{n,1} u_{n,2} u^*_{n,3} u^*_{n,4}\rangle\rangle = \langle u_{n,1} u_{n,2} u^*_{n,3} u^*_{n,4}\rangle - 2\langle u_{n,1} u^*_{n,2}\rangle^2 = -v_n^4\{4\}\,. \tag{49}$$

Double angle brackets denotes the cumulant. Problem is that the statistical errors are greater than in the case of event plane method and sometimes, the fourth power can be negative due to fluctuations.

Another modification of this method is using mixed harmonics. This method was used at RHIC to suppres the nonflow at directed flow measurements. Three-particle correlations were used:

$$\langle u_{n,1} u_{n,2} u^*_{2n,3}\rangle = v_n^2 v_{2n}\,. \tag{50}$$

3.1.2.5 Lee-Yang Zeros method

This method is basically all-particles correlation method. The origin is rooted in the Lee and Yang suggestions for detecting liquid-gas phase transition. The main advantage of this method is its nonflow independence for all orders. The main idea of this method is finding so-called *generating function* - a complex function - and its zero-point.

First, we will use the 2^{nd} harmonic flow vector $\overrightarrow{Q_2}$ projection to an arbitrary laboratory angle θ:

$$Q_2^\theta = \sum_{j=1}^{M} w_j \cos\left[2(\Phi_j - \theta)\right]\,. \tag{51}$$

The sum goes over all particles with angles Φ_j and weights w_j. The angle θ is usually estimated from five equally spaced values in order to minimize the effect of the detector acceptance. The generating function can be written as

$$G_2^\theta = \left| \langle \prod_{j=1}^{M} [1 + irw_j \cos(2(\phi_j - \theta))] \rangle \right| . \tag{52}$$

r denotes a variable along the imaginary axis of the complex plane. The zero-point of function G_2^θ, denoted as r_0^θ, is related to the flow as

$$v_2 = \langle \frac{j_{01}}{r_0^\theta} \rangle / M \, , \tag{53}$$

where j_{01} is first root of Bessel function and M denotes multiplicity.

Disadvantage of this method is high computational requirement, since the generating function has to be calculated for all values of r. The generating function can be also calculated as

$$G_2^\theta = \left| \exp\left(irQ_2^\theta \right) \right| , \tag{54}$$

but this approach works well only for v_2. Higher harmonics is better to calculate using eq. (52), since it better suppresses the effect of auto-correlation.

3.2 Nonflow and flow fluctuations

Thorough the previous paragraphs we mentioned nonflow contributions and flow fluctuations. Since all the introduced methods are just approximate and since we cannot measure everything, we have to take *nonflow contribution* δ_n and *flow fluctuations* σ_{vn}^2 into account.

Nonflow is mainly produced by intristic correlations between particles. Considering two particles, the nonflow contribution δ_n is defined:

$$\langle \cos(n(\Phi_i - \Phi_j)) \rangle = \langle v_n^2 \rangle + \delta_n \tag{55}$$

3.2 Nonflow and flow fluctuations

It is evident that nonflow is not dependent on the reaction plane. It is influenced by jet production, momentum conservation, Bose-Einstein correlations or resonance decay. Nonflow effects increase with transverse momentum and with centrality. More central collisions imply bigger contributions of hard parton collision and stronger radial flow. Data suggest that nonflow is dominant in collisions with centrality higher than 80% [18]. Its contribution can be minimized by using rapidity gaps between charged particles or by selecting correlated particles according to their charge. Nonflow computation gets more difficult with increasing number of correlated particles. Reminding equations (49) and (50), nonflow is the reason why multi-particle correlations are used. However, not all the effects can be removed using multi-particle correlations, and we have to choose the right method according to prevalent causes of nonflow.

Flow fluctuations σ_{vn}^2 are defined as:

$$\sigma_{vn}^2 = \langle v_n^2 \rangle - \langle v_n \rangle^2 \,. \tag{56}$$

Main contribution to flow fluctuations are random configurations in the overlapping regions of colliding nuclei. Even though it is very complicated to measure fluctuations themselves, it is simple to detect them. Due to the definition (56) and using the correlation method, we obtain the results directly.

Event plane method dependence on flow fluctuations is more complicated. It depends on the reaction plane resolution and ranges from $v_2\{EP\} = v_2\{2\} = \langle v^2 \rangle^{1/2}$ to $v_2\{EP\} = \langle v \rangle$.

Comparison of different methods used for establishing v_2 in respect to event-plane method is depicted in the fig. 14. The presented data are obtained from $\sqrt{s_{NN}}$=200 GeV Au-Au collisions. The values are shown for event plane method, method using random and pseudorapidity subevents, for scalar-product method, two- and four-particle cumulant method, q-distribution and for Lee-Yang Zeroes method using both equations (52) and (54). Different methods may lead to different results. One has to be careful when choosing the method.

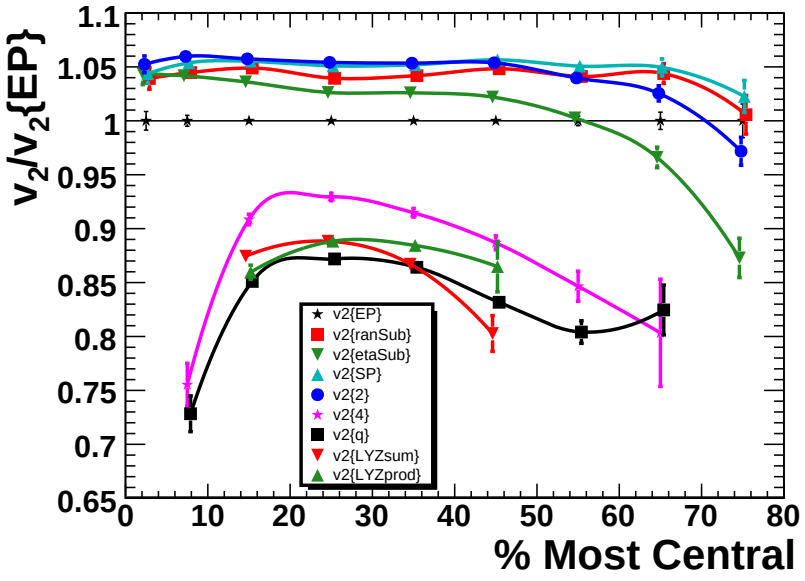

Figure 14: Comparison of calculation methods for $v_2/v_2\{EP\}$ versus centrality. Taken from [16].

3.3 Experimental results

Figure 15 reflects measurements of $v_n = v_n(p_T)$ for all charged particles done by experiment ALICE at LHC [18]. There were Pb-Pb collisions at $\sqrt{s_{NN}}$=2.76 TeV. It is obvious that elliptic flow is highly centrality-dependent. As expected, triangular flow is not significantly centrality-dependent[8]. There is a clear difference between the results obtained by using different methods: $v_n\{EP\}$ denotes event-plane method while $v_n\{4\}$ denotes four-particle cumulant method. It appears that the flow fluctuations are positive for event-plane method, while for cumulant method they are negative. This effect is more relevant in the area for $p_T < 7$ GeV. In the case of quadrangular flow, both elliptic and quadrangular symmetry plane are considered. It is obvious from the figure that v_4 evinces strong centrality dependence, when probed by the correlation with the Ψ_2 plane, in contrast to the v_4 in the Ψ_4 plane, where the centrality dependence is very weak. This centrality independence suggest strong

[8]Worth emphasizing is the difference in the vertical axis values between the upper and lower line.

connection to flow fluctuations.

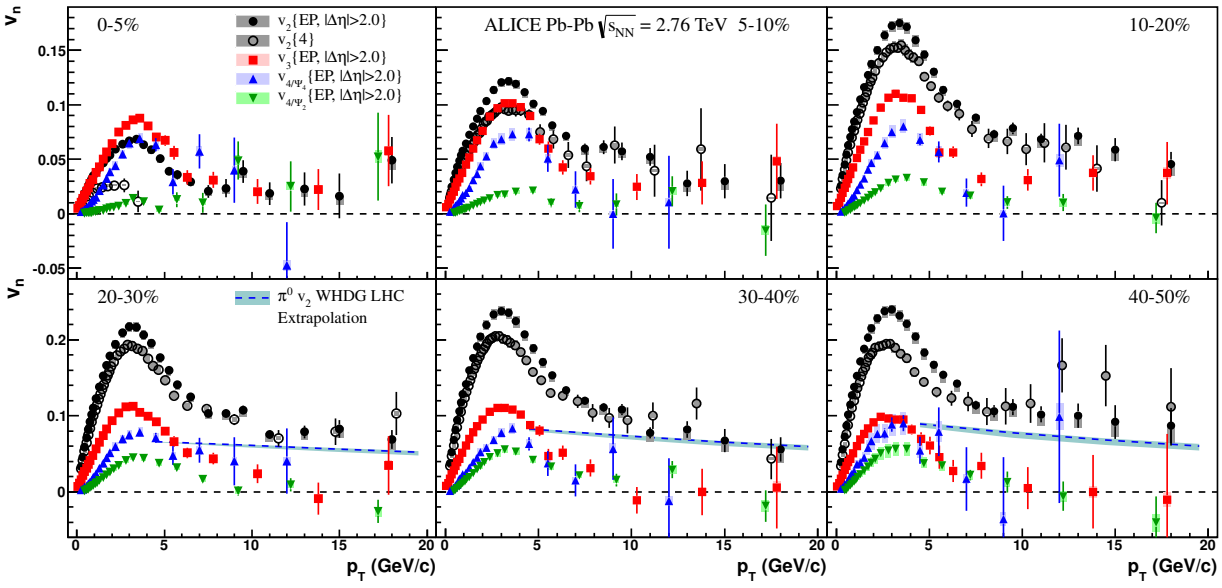

Figure 15: ALICE $v_n = v_n(p_T)$ measurements for unidentified charged particles up to $p_T = 20\,\text{GeV}$. The v_3 and v_4/Ψ_2 markers are shifted along the horizontal axis for better understanding. Boxes are systematic errors, error-bars denote statistical uncertainty. Taken from [18].

The relation of the relative difference between event-plane method and four-particle cumulant method is represented in the fig. 16. This difference is expressed as

$$\sqrt{\frac{v_2\{EP\}^2 - v_2\{4\}^2}{v_2\{EP\}^2 + v_2\{4\}^2}}\,. \tag{57}$$

For small nonflow, this quantity is proportional to $\sigma_{v_2}/\langle v_2\rangle$. For mid-centrality, this ratio is minimal, while for central collisions it is close to one. Interesting is the fact that for centrality class higher than 5% the relative flow fluctuations are p_T independent. This implies a common origin of flow-fluctuations. For the most central collisions, the ratio increases from $p_T = 1.5\,\text{GeV}$. This indicates the biggest nonflow effects.

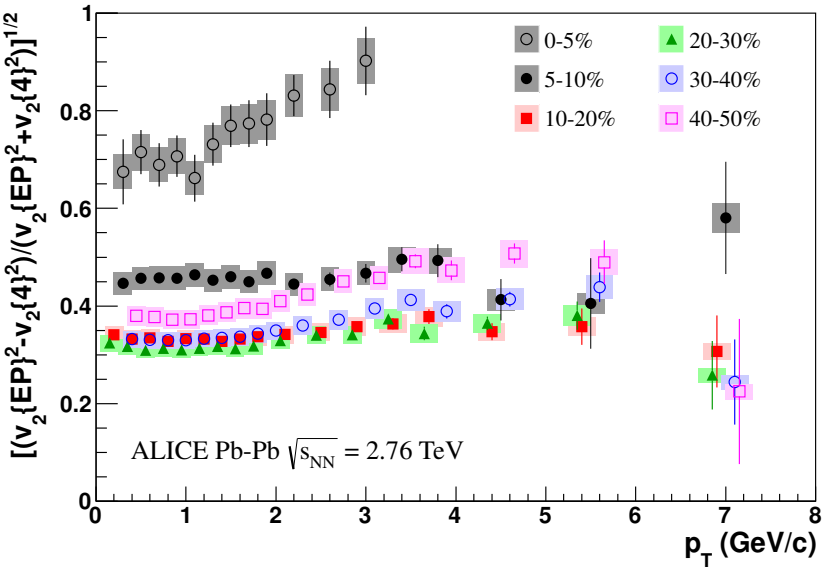

Figure 16: ALICE relative flow fluctuations $\sqrt{\frac{v_2\{EP\}^2-v_2\{4\}^2}{v_2\{EP\}^2+v_2\{4\}^2}}$ measurements for unidentified charged particles up to $p_T = 8\,\text{GeV}$ for different centrality classes. Boxes are systematic errors, error-bars denote statistical uncertainty. Taken from [18].

4 Toy Model

Our task was to make a toy model for generating a profile of the azimuthal angle distribution, using Monte Carlo mehtod, to produce 5000 pions of transverse momentum $p_T = 500$ MeV. Next step was to compute the n^{th} differential flows using correlations and histogram. The aim of this task was to learn to work in programming languages C, C++, acquire working knowledge in ROOT, working with random number generators and deeper understanding of methods discussed in section 3 acquired by their implementation.

I considered differential flows up to the 5^{th} degree. The distribution used for generating particles is described by eq. (37). For the analzsis of Monte Carlo data we used the *event plane method* and *correlation method*. Moreover, we analyzed the data from the model DRAGON.

4.1 Theoretical background

Normally, Monte Carlo simulation uses a random number generator generating uniformly distributed numbers in the interval $(0, 1\rangle$; denoting $x \sim U(0, 1)$. However, one usually needs to produce non-uniform distributions. There are several methods how to do so. The simplest distributions can be integrated analztically, e.g. exponential distribution. Another possibility how to create a non-uniform distribution is to use *rejection method* [23]. This method is very similar to numerical computation of integrals. Now, we will look at both methods in detail.

4.1.1 Transformation method

This method is based on direct analytic integrations of the desired distribution $p(x)$. Suppose we are able to generate uniformly the deviate x and that we want to generate distribution $p(y)$. We apply usual probability transformation from $p(x)$ to $p(y)$:

$$|p(x)dx| = |p(y)dy|\,,$$
$$p(y) = p(x)\left|\frac{dx}{dy}\right|\,.$$

Because $x \sim U(0,1)$, we may write

$$p(y)dy = \left|\frac{dx}{dy}\right| dy\,.$$

This immideately leads to

$$\begin{aligned} p(y) &= \left|\frac{dx}{dy}\right|\,, \\ x = F(y) &\Rightarrow y(x) = F^{-1}(x)\,. \end{aligned} \tag{58}$$

where $F(y)$ denotes primitive function to $p(y)$. This method is simple and fast. The problem here arises from the equations (58). Both the integral of $p(y)$ and the inverse function of $F(y)$ may not be analytically solvable and any approximate method requires more computation time and is only approximate.

4.1.2 Rejection method

We will assume we need to generate numbers with certain distribution function $p(x)$. We will choose a *comparison function* $f(x)$. Its function value is bigger than that of distribution $p(x)$ value on its whole domain D_p. Of course, $D_p \subset D_f$. Then, we uniformly populate the area below the function $f(x)$, denoting the points $x = [u, i]$. We compute value of $p(u)$ and $f(u)$. If $i > \frac{p(u)}{f(u)}$, we will *reject* number u and generate new ones until the condition $i < \frac{p(u)}{f(u)}$ is satisfied. The ratio of rejected to accepted numbers is equal to the ratio of the area between $f(x)$ and $p(x)$ to the area under $p(x)$. An illustration is shown in fig. 17.

The advantage of this method is its simplicity. However, its efficiency highly depends on the choice of the comparison function $f(x)$. If we can make a good approximation of the distribution $p(x)$, the count of rejected numbers will be small and this method is very efficient. On the other hand, such a good approximation does not always exist on the whole D_p. Bad approximation leads to a large number of rejected numbers, which prolongs the computation time.

Since the distribution function has to have a maximum, because integration over its domain gives 1, is positive and continuous, it is always possible to make an upper estimate

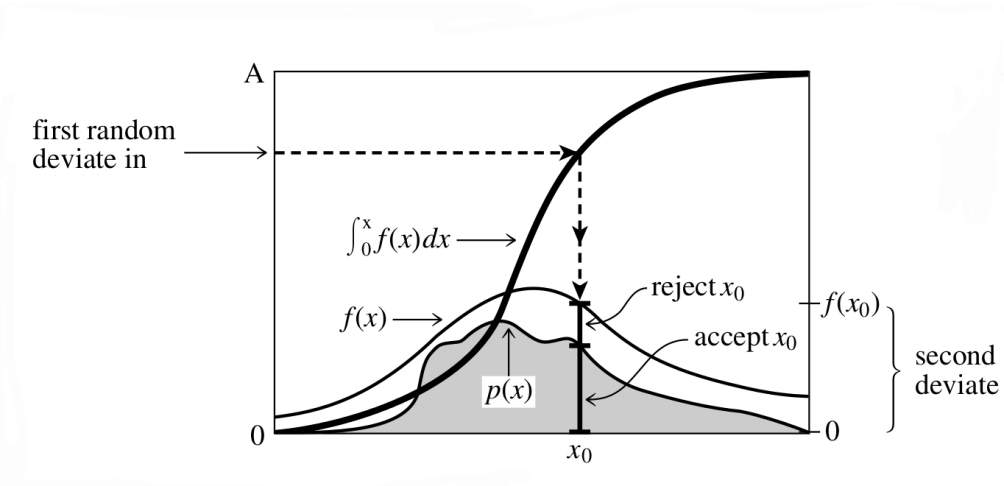

Figure 17: Rejection method illustration. Taken from [23].

by function $f(x) = \max_{x \in D_p}\{p(x)\}$, making '*rectangle*' around the desired distribution. The suitability of this estimation highly depends on the $p(x)$. The problem is that this works only for distributions that are non-zero at finite interval.

4.2 The program

4.2.1 Particle identification

In our program, we sticked to the Monte Carlo numbering scheme of particle species according to [24]. Particles are marked by seven digits, positive numbers denotes particles, negative anti-particles. In principle, the digits reflect spin, flavor and other quantum numbers. Quarks are denoted by a single digit, leptons and bosons by two-digit numbers, mesons by three-digit numbers (however, to distinguish same particles in different state, they can have more digits, as well as baryons) and baryons by four digits.

4.2.2 Random number generator

Since the built-in C++ random number generator is not reliable enough (most significantly, it is a linear congruential generator), the program uses the random number generator suggested

by [23]. The structure allows the usage of three different random results: 64-bit unsigned integer, 32-bit unsigned integer and, most importantly, double-precision float; values 0.0 - 1.0.

4.2.3 p_T distribution

The goal is to generate transverse momentum p_T and azimuthal angle Φ. The p_T distribution is

$$\frac{dN}{dp_T} = C p_T e^{-\frac{p_T}{T}} , \tag{59}$$

where N denotes number of particles, T is a parameter. C denotes normalization constant. In our case, we choose $T = 400\,\mathrm{MeV}$.

The reason why it is not possible to use transformation method is following. From equations (58) and (59):

$$x = C \int dp_T \, p_T \, e^{-\frac{p_T}{T}} = -CT(T + p_T)e^{\frac{-p_T}{T}} \tag{60}$$

The factor C reflects normalization: we generate $x \in \langle 0, 1)$ and x is dimensionless. In our case, $C = -1/T^2$.

The inverse function of $x\, e^x$ is not analytically solvable. It can be expressed in terms of *Lambert function* W:

$$p_T(x) = -T \left(1 + W\left(\frac{x}{e}\right)\right) . \tag{61}$$

This function may be approximated by several methods, for instance see [25]. One of the simplest approaches of computing $W(x)$ is

$$W(x) = \ln\left(\frac{x}{\ln\left(\frac{x}{\ln(\ldots)}\right)}\right) . \tag{62}$$

This approach is simple, for small number of iterations it is even fast. We chose initial $W_0(x)$, followed by iteration according to $W_{n+1}(x) = \ln(x/\ln(W_n(x)))$. Computation was done at an ordinary laptop, with Intel® Core^{TM} i3 Processor with clock speed 2.13 GHz. However, it was not fully used just for this computation, making the following data good for

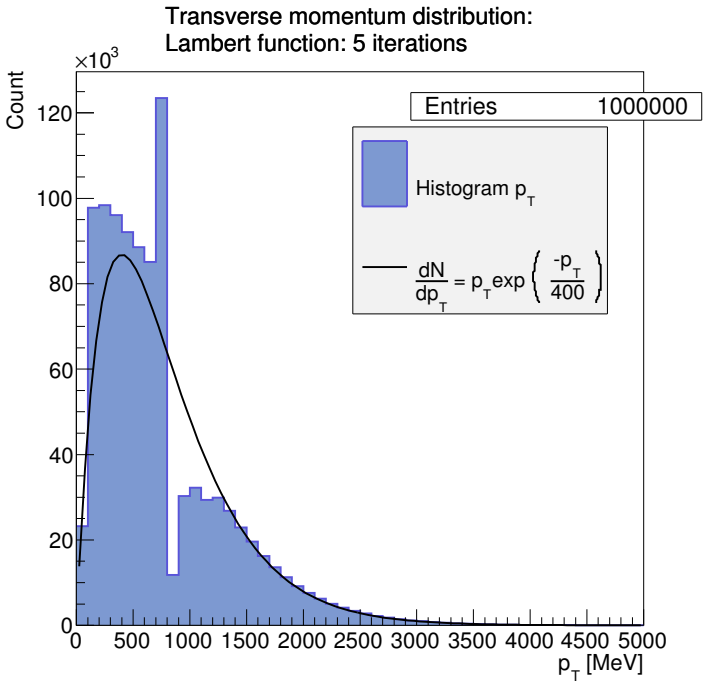

Figure 18: p_T histogram using Lambert function (62), computed with 5 iterations, $W_0 = 0.1$.

comparison, not as absolute numbers. For one million generated numbers, this method for 5 iterations takes 0.35 s. For 100 iterations, the needed time rises up to 5.36 s. Moreover, the reliance of this method strongly depends on the number of iterations. An example is shown at figures 18, 19, 20 and 21. Figure 18 is an histogram for 5 iterations, the black line illustrates desired shape of distribution (59), where $T = 400\,\mathrm{MeV}$. It is obvious that 5 iterations are not precise enough. However, it can be successfully used for generating higher p_T. The big discontinuity in fig. 18 is caused by the problem in around $2T$ because of the limit of eq. (62).

Figures 19 and 20 represents p_T distribution computed using Lambert function W with 10 and 20 iterations. The histograms are fitted with function $p_T\ exp\left(p_0 + \frac{p_T}{p_1}\right)$, p_0 is scale-parameter, p_1 should be equal to T. The increasing error of the fit is caused by the width of the bins; there are 50 bins in the histogram. For 20 iterations, the computing time rises to 1.12 s, making this method slower than the rejection method. The same method, computed

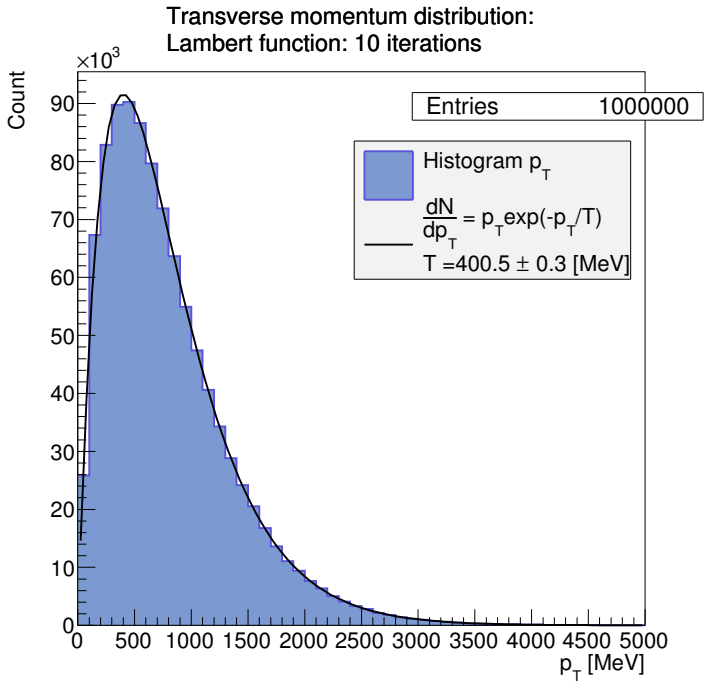

Figure 19: p_T histogram using Lambert function (62) computed with 10 iterations.

with 100 iterations, is shown in the fig. 21. There are 100 bins, the fitted T is acceptable. As mentioned, the computing time is very long and the precision is not very high.

Another interesting fact is the dependence on $W_0(x)$. For higher number of iteration, choosing some small number (0.1 is sufficient) is an approximation good enough. It does not significantly affect the resulting distribution, choosing better first-guess slows down the computation and for 10 iteration the difference is negligible. However, for 5 iterations, using the *Branch-point* expansion suggested in [25] only up to the first coefficient leads to much better results; see fig. 22 in contrast with fig. 18. This one operation does not significantly slow down the algorithm. However, the distribution still evinces small shift from the distribution around $p_T = T$.

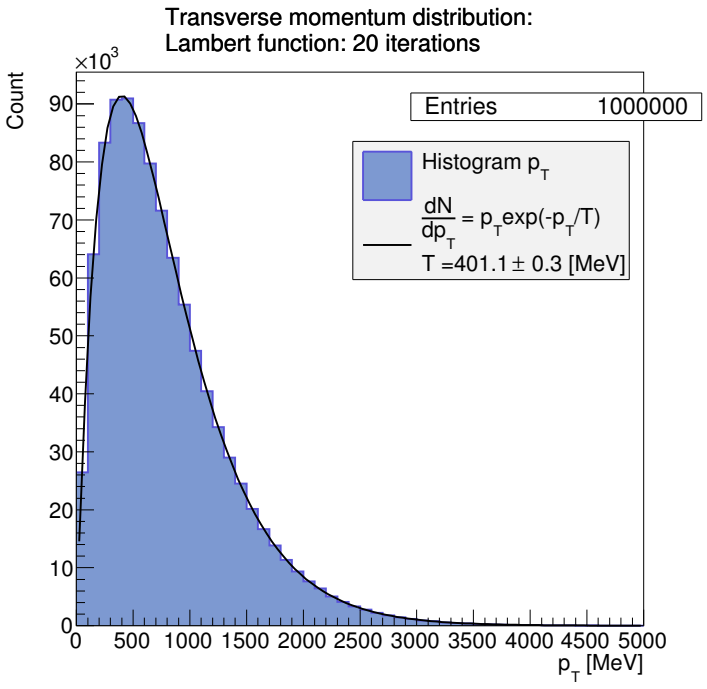

Figure 20: p_T histogram using Lambert function (62), computed with 20 iterations.

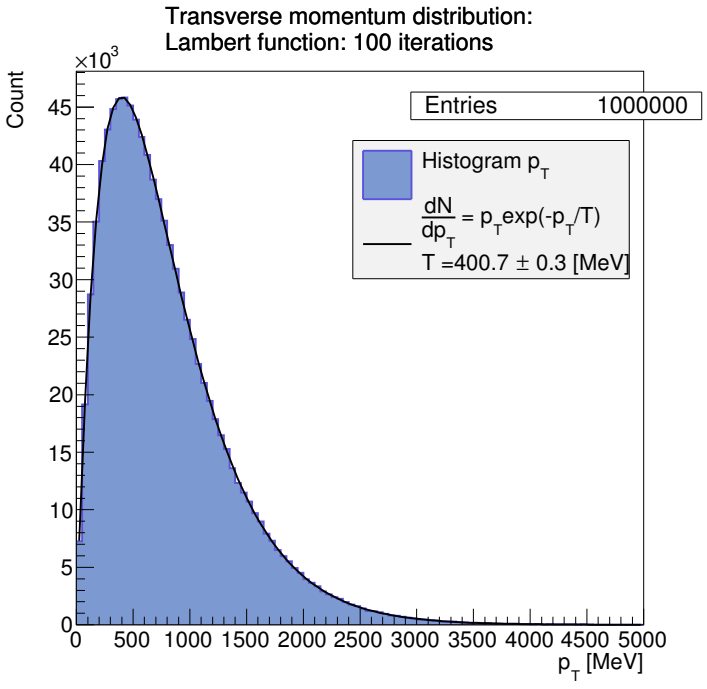

Figure 21: p_T histogram using Lambert function (62), computed with 100 iterations.

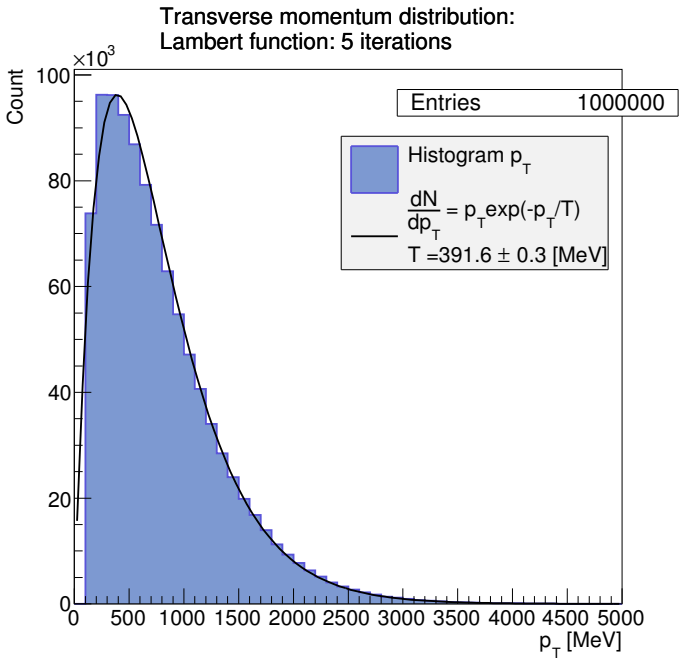

Figure 22: p_T histogram using Lambert function (62), computed with 5 iterations, initial $W_0(x) = 1 - \sqrt{2(1+xe)}$.

4.2.4 Azimuthal angle distribution

The azimuthal angle Φ is generated according to the distribution

$$\frac{dN}{d^2p_T} = \frac{dN}{2\pi p_T dp_T}\left[1 + \sum_{n=1}^{\infty} 2v_n \cos(n(\Phi - \Psi_n))\right] . \tag{63}$$

In this case, the rejection method can be used without a problem. Equation (63) depends on cosine, whose range lies in the interval $\langle -1, 1\rangle$. We can even use the 'rectangle' mentioned in 4.1.2. Since angles are relevant only in the interval $(0; 2\pi\rangle$, we can generate any angle simply by multiplying the uniformly distributed x by 2π. Hence, the ratio of rejected to accepted numbers is acceptable, $N_a/N_g \simeq 0.43$. Of course, this ration depends on the coefficients v_n.

We used coefficients up to pentagonal flow: $v_1 = 0.1$, $v_2 = 0.05$, $v_3 = 0.03$, $v_4 = 0.01$ and $v_5 = 0.005$. Ψ_n is generated randomly for every event. An example of generated angles is in the fig. 23. For the sake of illustration, we generated one event with 100000 particles, which

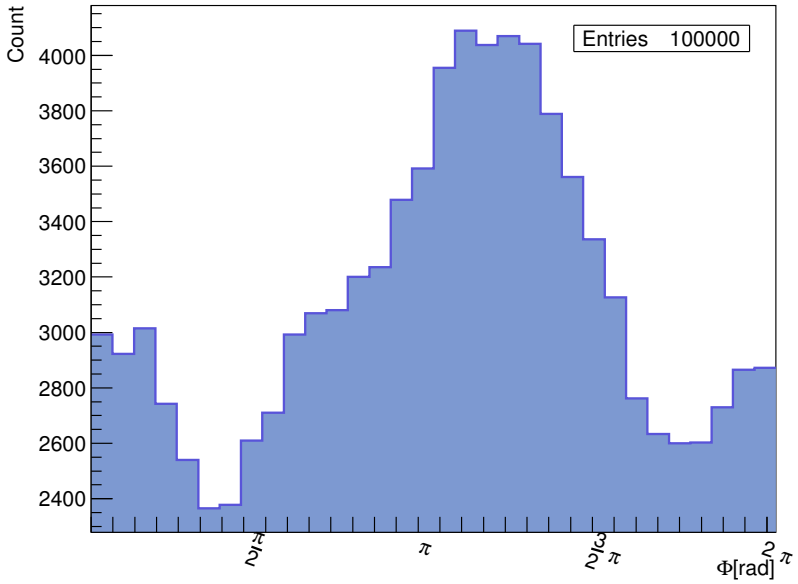

Figure 23: Azimuthal angle Φ histogram according to eq. (63). Used coefficient are in the table 1.

	1	2	3	4	5
v_n	0.1	0.05	0.03	0.01	0.005
Ψ_n [rad]	3.6349	0.414679	2.04821	5.03192	1.92727

Table 1: Azimuthal angle distribution coefficients

is clearly unrealistic, but provides sufficient statistics to show the features of the distribution. For better illustration we include histogram in polar coordinates.

4.2.5 Analysis

We produced 5000 events, consisting of 5000 pions, using the methods described above. For generating p_T, we chose the lambert function, computing it as 10 iterations with initial $W_0(x) = 1 - \sqrt{2(1+xe)}$. We analyzed the data using cumulant method and event plane method. The results from correlation method are very good. As mentioned in the section 3.1.2, cumulant method is a good aproximation assuming small p_T dependence, negligible nonflow and constant flow fluctuations. Our program meets all of this require-

ments. For elliptic flow, there were none negative v_2^2. After root extracting, we obtained $v_1 = (0.1002 \pm 0.0001)$, $v_2 = 0.0496 \pm 0.0001$, $v_3 = 0.0299 \pm 0.0002$, $v_4 = 0.0098 \pm 0.0002$ and $v_5 = 0.0048 \pm 0.0003$. The results are in the fig. 24. As can be seen, the results for v_4 and v_5 are not very precise. However, due to larger error, it meets our initial parameters.

Results from event plane method are not as good as from cumulant method. However, as can be seen in fig. 25, modes of the results are close to the desired v_n. This is probably caused by the fact that we did not consider subevents, required for computing event plane resolution $\Re_n$, meaning our obtained v_n stand for v_n^{obs}. Moreover, using p_T as a weight in eq. (38) is a good approximation up to 2 GeV and many of the simulated particles have higher p_T. Moreover, our p_T and Φ distributions are not related. The results are suprisingly good for $v_5 = 0.0051 \pm 0.0001$.

Worth emphasizing is the fact, that obtained directed and elliptic flows are integrated flows: p_T binning results in big statistical uncertanity, since there are not enough produced particles.

4.3 Program documentation

The program is written in C++. It was written using Unix operating system. It consists of five header files: `nr3`, taken from [23], as a source for the random number generator. Generator itself is defined in `generator.cpp`. Toy model generator of azimuthal angle and transverse momentum is stored in `toymodel.cpp`. Analysis takes place in `list.cpp`, in `list.h` we defined one-way linked list and its basic operations. The main source is `main.cpp`.

Parameters can be set in the `parameters.h`. We define the maximum order of Fourier decomposition Fn, applied both for analysis (analyses all v_n up to Fn) and Monte Carlo part. The output, however, has to be corrected manualy in corresponding functions. The reason we did so is for simple constriction/extension of the program. We also set the parameter T in eq. (59), denoted as TT. Furthermore, we define number of generated events ($NoEvents$) and number of particles in one event ($NoParticles$). Moreover, the names of toy model output, analysis input and output are required. Since we need to analyse v_n for different

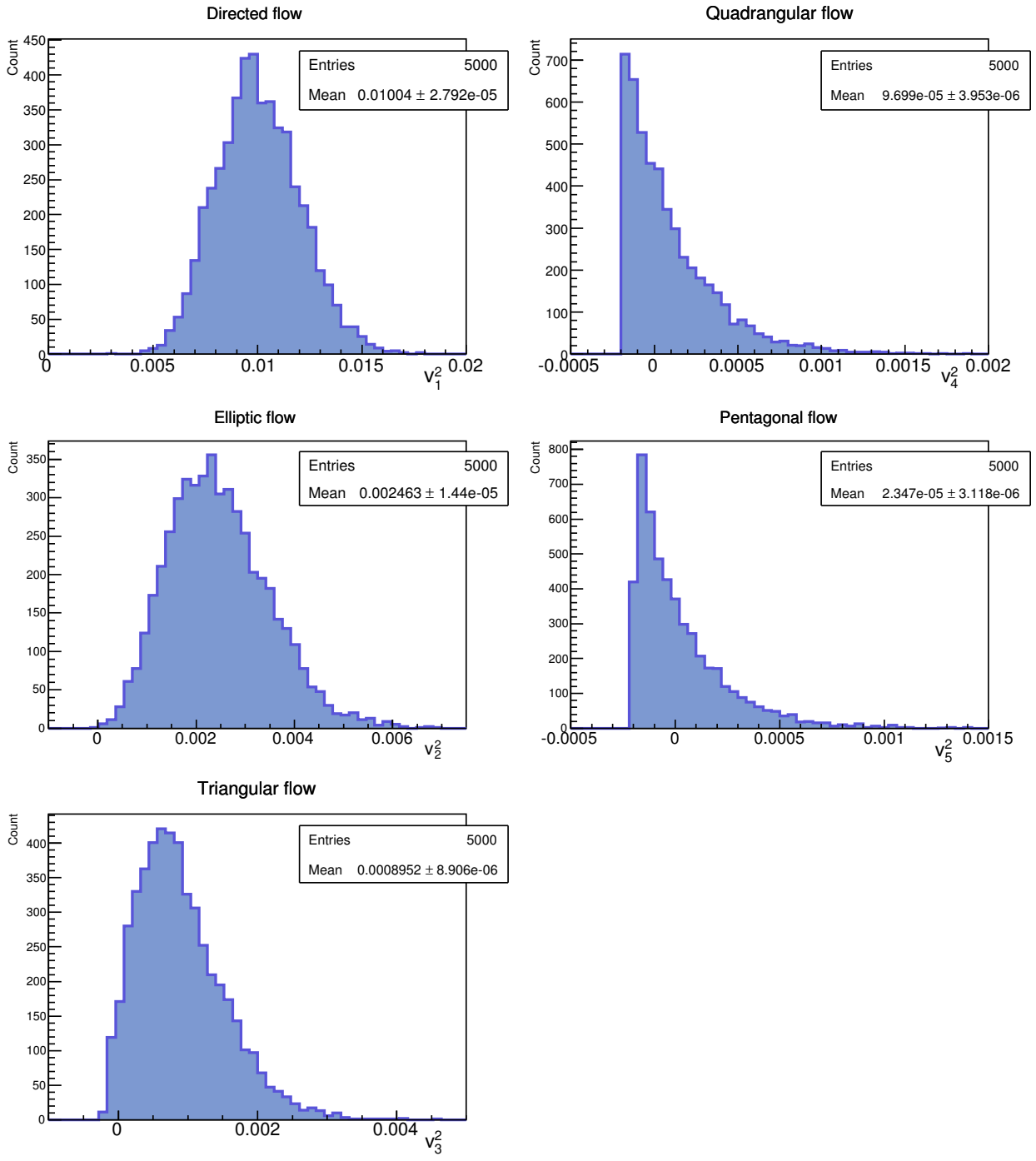

Figure 24: Correlation method: v_1^2 and v_2^2 histogram from 5000 events for toy model produced pions.

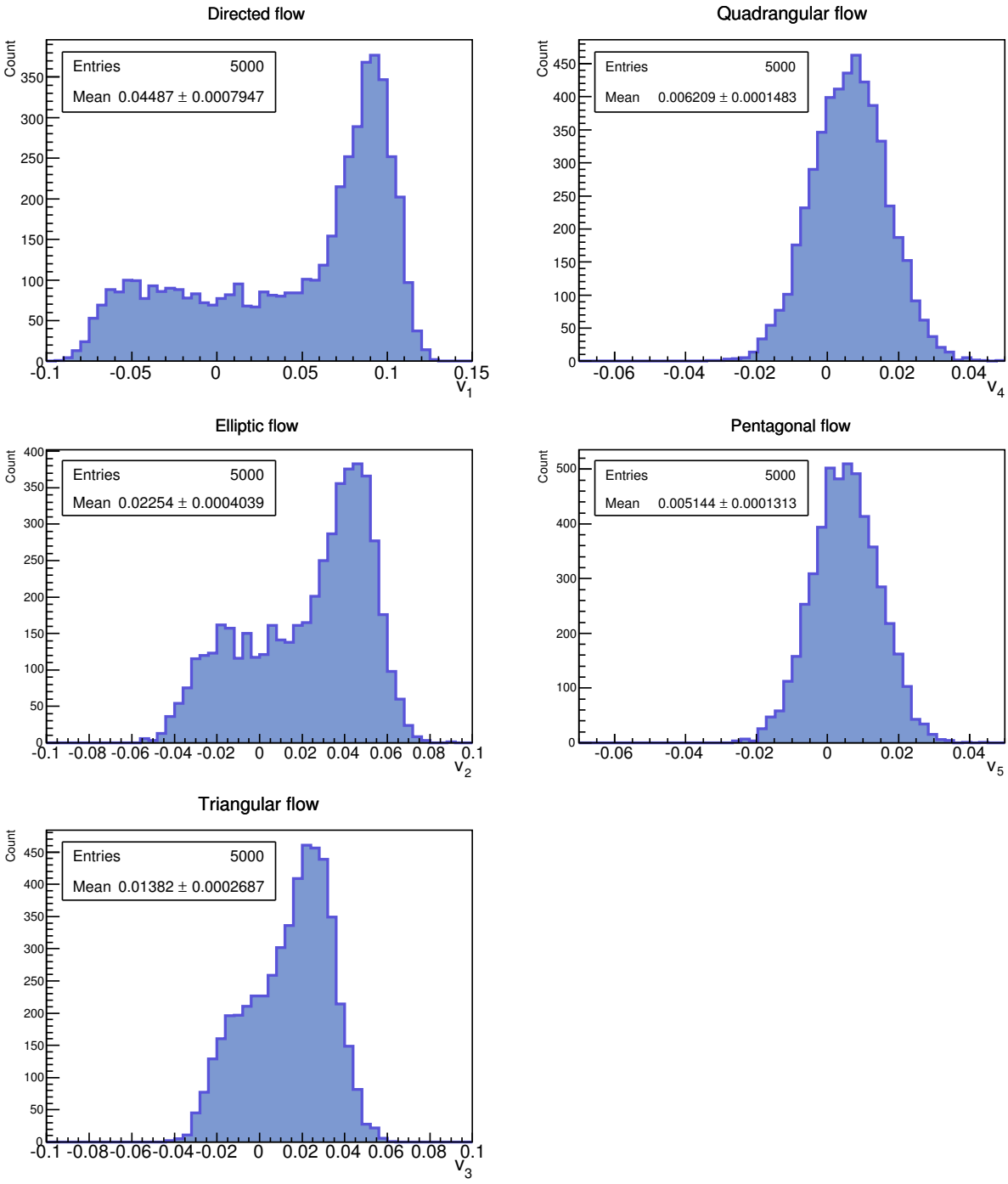

Figure 25: Event plane method: v_1 and v_2 histogram from 5000 events for toy model produced pions.

particle species, parameter *number* decides about the type of particles. For future extension, other numbers can be defined. However, we have to extend also the function `id_number` in `list.cpp`. Furthermore, there is parameter *LOOP* in `toymodel.cpp`, regarding several testing functions.

We add `makefile` for simple compilation. After the launch of the program, user is required to choose between angle and momentum generation, cumulant method analysis, event plane method analysis or analysis by both methods. After choosing, control sequence is written, confirming it by enter.

4.4 DRAGON

DRAGON is a Monte Carlo generator of the final state of hadrons emitted from an ultrarelativistic nuclear collision. The name comes from DRoplet and hAdron GeneratOr for Nuclear collisions. It is similar to THERMINATOR I and II, but it is extended by the emission of fireball fragments. Those fragments may arise from bulk viscous force or from spinodal decomposition. The computation of fragments is based on blast wave model and azimuthally non-symmetric fireballs. It is written in C++, output is set to standard OSCAR1999 format, but there are many possibilities how to simply change it. In our case, the output was number of event, id number of particle according to the standard particle identification [24], transverse momentum and azimuthal angle. This particular input is required even for our analysis program.

The probability of generating particle with momentum p for space time point x is given by the emission function

$$S(x,p)d^4x = \frac{2s+1}{(2\pi)^3} m_T \cosh(y-n) \exp\left(-\frac{p^\mu u_\mu}{T_k}\right) \Theta(1-\tilde{r}(r,\phi)) H(\eta) \delta(\tau-\tau_0) d\tau\tau d\eta r dr d\phi \,, \tag{64}$$

where s reflects spin degeneration, $H(\eta)$ reflects space-time rapidity profile of the fireball. We generated 5000 events with kinetic freeze-out temperature 0.09 GeV, chemical freeze-out temperature 0.156 GeV. This parameters are motivated by LHC results for Pb-Pb

collisions. We put zero baryo-chemical potential as well as strangeness potential. The dN/dy was set as 1500. We stated the flow anisotropy parameter ρ_2 as 0.1 and spatial anisotropy parameter a as 0.95. These parameters define the space anisotropy. Assuming flow velocity $u_\mu = (\cosh\eta\cosh\eta_t, \sinh\eta_t\cos\phi_b, \sinh\eta_t\sin\phi_b, \cosh\eta_t\sinh\eta)$, we may write $\eta_t = \sqrt{2}\rho_0\tilde{r}(1 + 2\rho_2\cos(2\phi)_b)$, where $\tilde{r} = \sqrt{\frac{r^2\cos^2\phi}{R_x^2} + \frac{r^2\sin^2\phi}{R_y^2}}$. Using mean transverse radius of the ellipsiodal fireball R, $R_x = aR$ and $R_y = R/a$. This means that only elliptic flow is present. Detailed description can be found in [1].

4.4.1 DRAGON results

4.4.1.1 Cumulant method

First, we computed the mean $cos(n(\psi_i - \psi_j))$. We decided to calculate integrated v_n, because of insufficient multiplicity: considering p_T bining per 0.5 GeV, the obtained mean value was smaller than its error.

Best results evince pions. As can be seen, directed flow is very small, final result $v_1^2 = (48.1 \pm 0.3)^{-6}$ and $v_2^2 = (2.94 \pm 0.02)10^{-3}$, resulting in $v_2\{2\} = 0.0654 \pm 0.0002$. Results are in the fig. 26. Interesting are the results for directed flow, DRAGON is desined without its presence. We expect that non-zero v_1 is caused by statistical fluctuations.

Since the number of produced kaons is bigger than for Λ baryons or protons, the obtained results are less influenced by statistical errors. As can be seen in the fig. 27, final $v_1^2 = (0.06 \pm 0.01)10^{-3}$ and $v_2^2 = (3.54 \pm 0.03)10^{-3}$, resulting in $v_2\{2\} = 0.0595 \pm 0.0003$

Final obtained integrated v_1^2 and v_2^2 for protons is in fig. 28. Final $v_1^2 = (6 \pm 3)10^{-5}$. More promising results are those for v_2^2. As can be seen in the figure, main contribution of elliptic flow is around zero, some of it is even below zero. The final obtained $v_2^2 = (3.40 \pm 0.09)10^{-3}$, resulting in $v_2\{2\} = 0.0583 \pm 0.0008$.

Similar to protons, the multiplicity of Λ baryons is not sufficient enough to make any conclusions from the data. Results are in the fig. 29. The final $v_1^2 = (0.2 \pm 0.1)10^{-3}$ and $v_2^2 = (3.7 \pm 0.1)10^{-3}$, resulting in $v_2\{2\} = 0.0608 \pm 0.0008$.

4.4.1.2 Event plane method

We also analyzed the same sample of data using the event plane method. First, we obtained the mean $\cos(\Psi_n - \phi_j)$, which is denoted as v_n^{obs}. Then, we calculated the mean of v_n^{obs} and denoted is as v_n: $v_n = \langle v_n^{obs} \rangle$. As well as in the case of analyzing our generated particles, we should use the event plane resolution $\Re_n$, however, obtaining subevents from DRAGON would be too complex for our analysis. The results are $v_2 = 0.0307 \pm 0.0007$ for protons, $v_2 = 0.0348 \pm 0.0009$ for Λ, $v_2 = 0.0255 \pm 0.0005$ for kaons and $v_2 = 0.0230 \pm 0.0004$ for pions, as can be seen from the figures 30, 31, 32 and 33, respectively.

4.4.1.3 Comparison of the results

As can be seen in the fig. 34, the results are very different from each other. As well as it can be seen in the fig. 30, 31 and 32, it is probably caused by the inaccurate establishing of the v_2 from event plane method. Moreover, the nonflow or presence of the resonances may play its role. The results from event plane method are approximately two times smaller than the results from cumulant method. We suggest further studying of this phenomenon, for example by using four-particle correlation method.

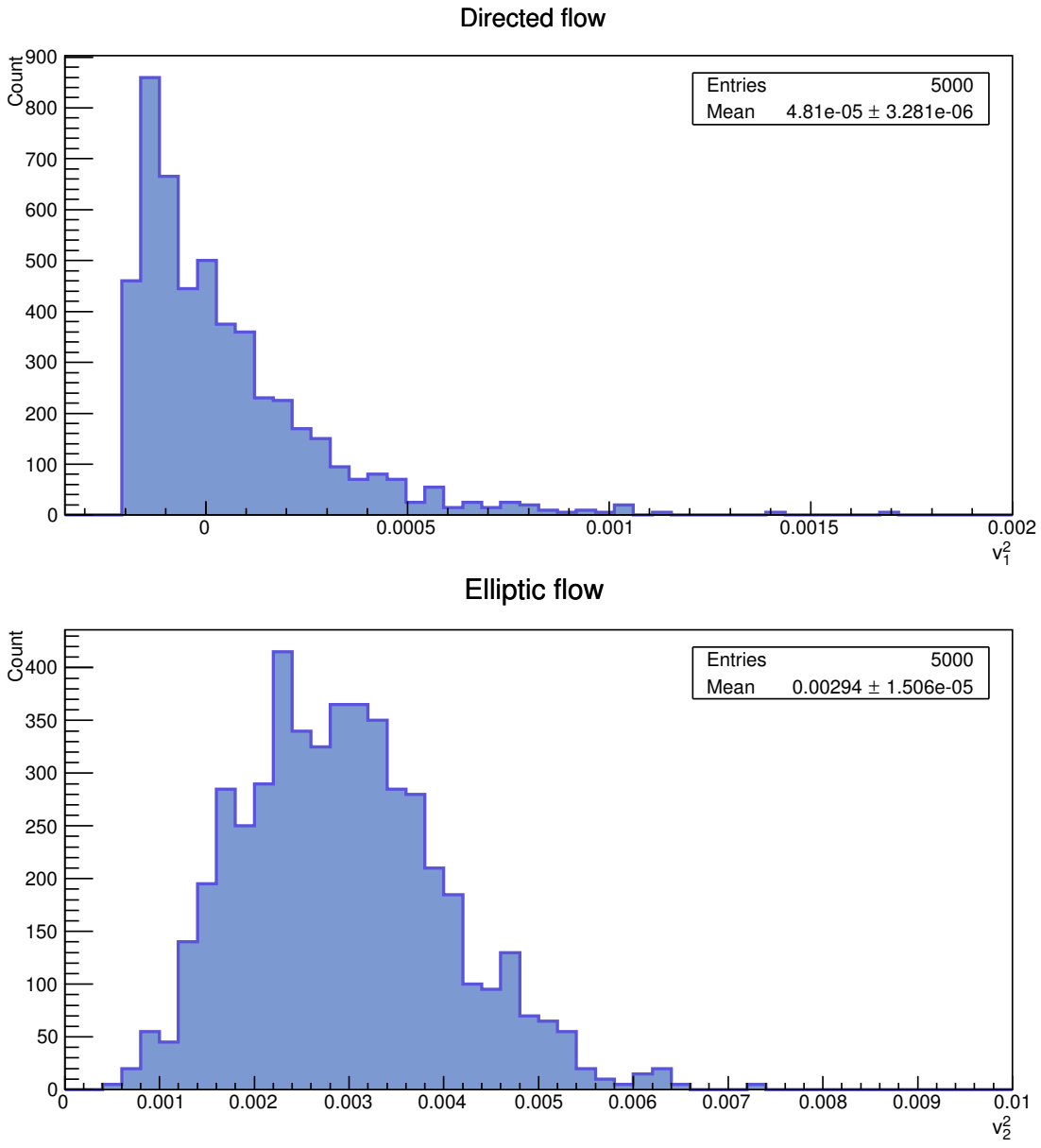

Figure 26: Correlation method: v_1^2 and v_2^2 from 5000 events for pions.

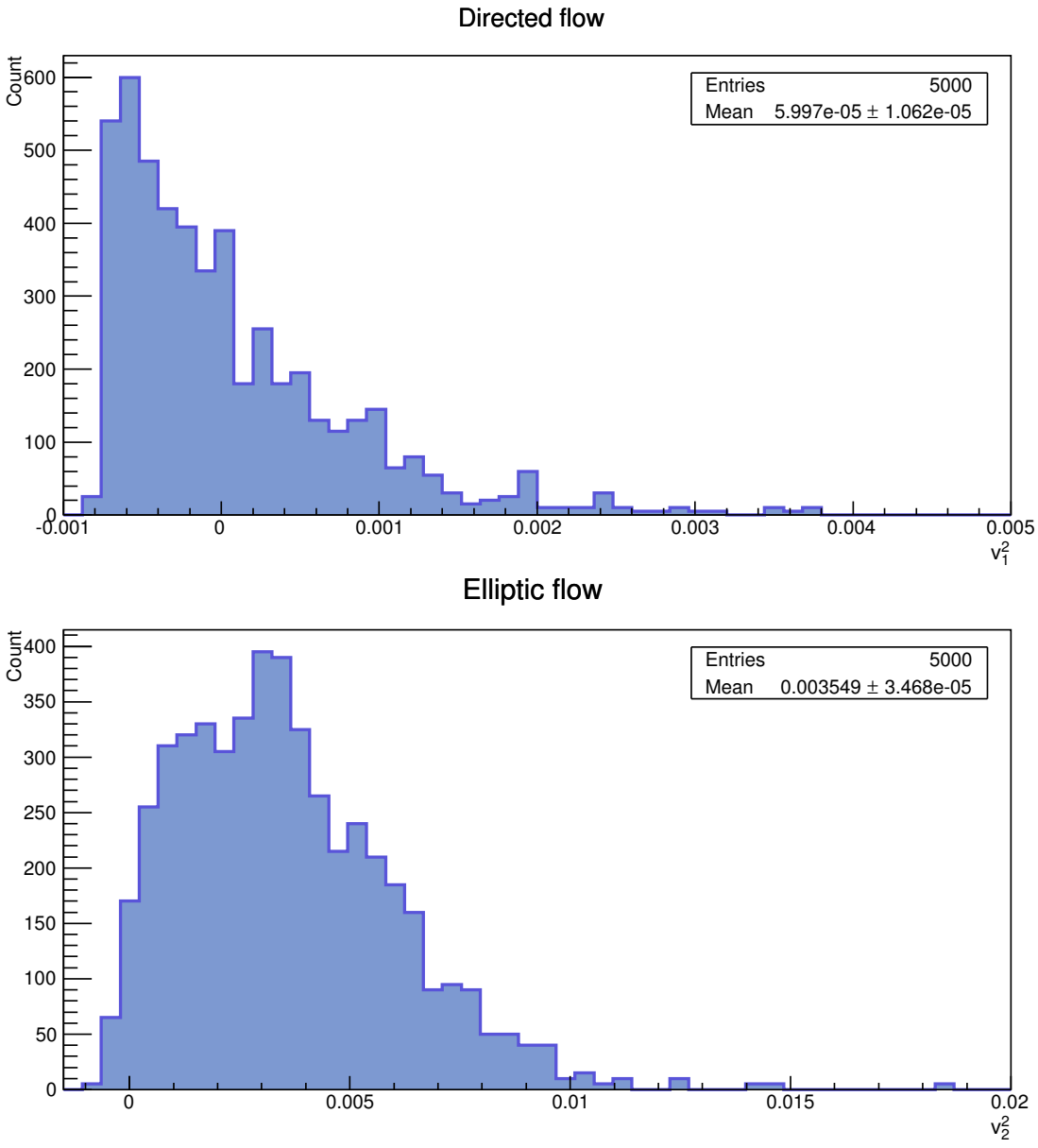

Figure 27: Correlation method: v_1^2 and v_2^2 from 5000 events for kaons.

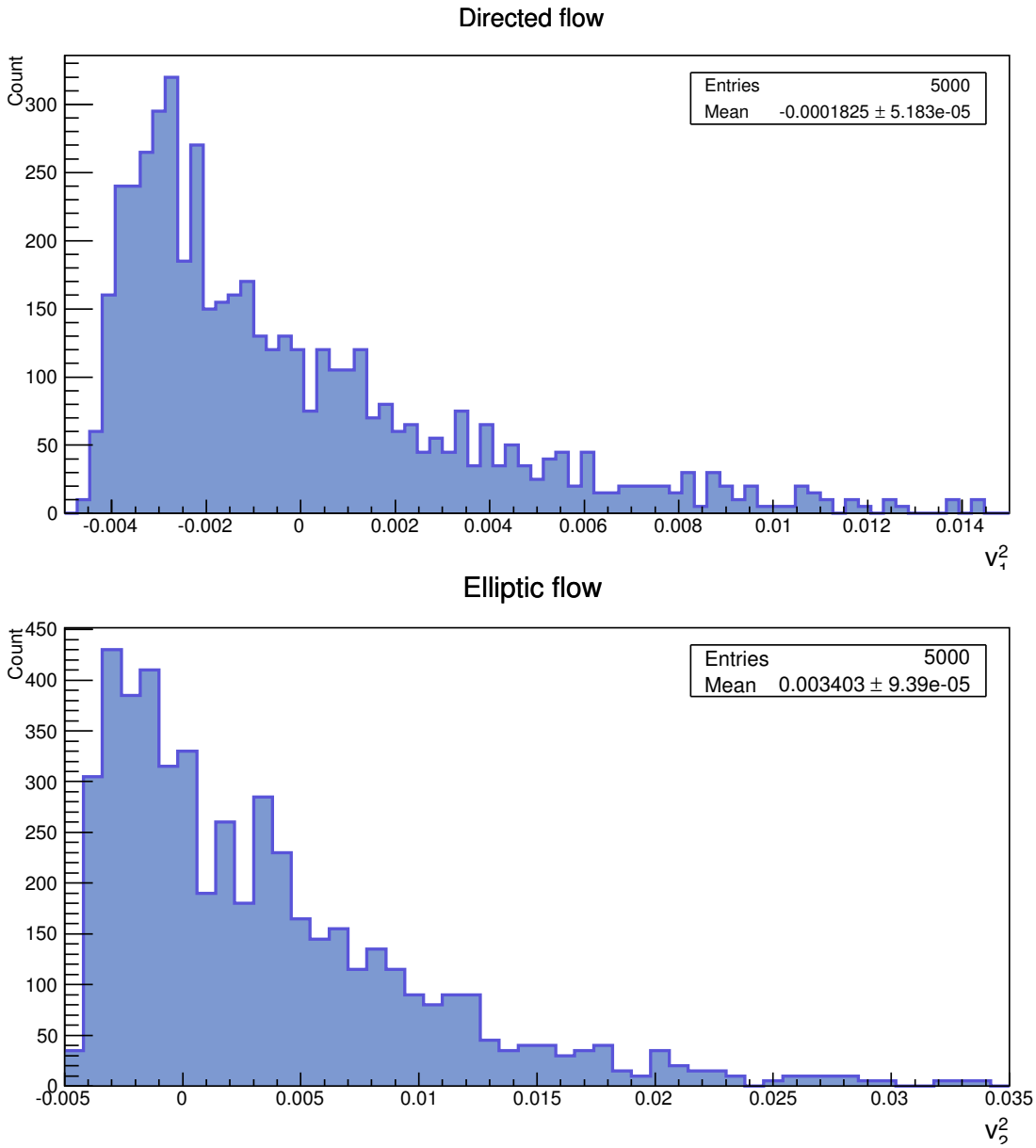

Figure 28: Correlation method: v_1^2 and v_2^2 from 5000 events for protons.

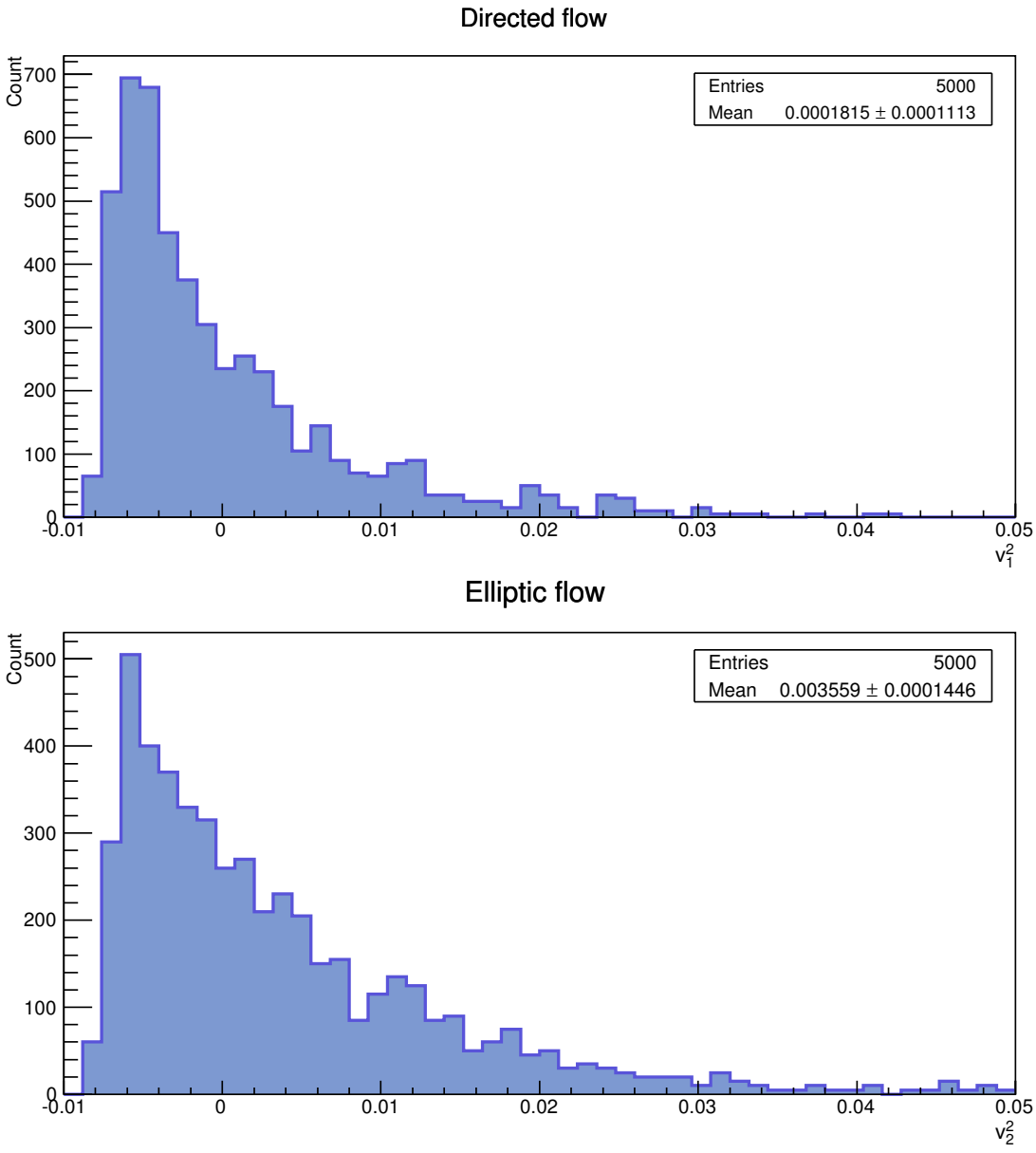

Figure 29: Correlation method: v_1^2 and v_2^2 from 5000 events for Λ baryons.

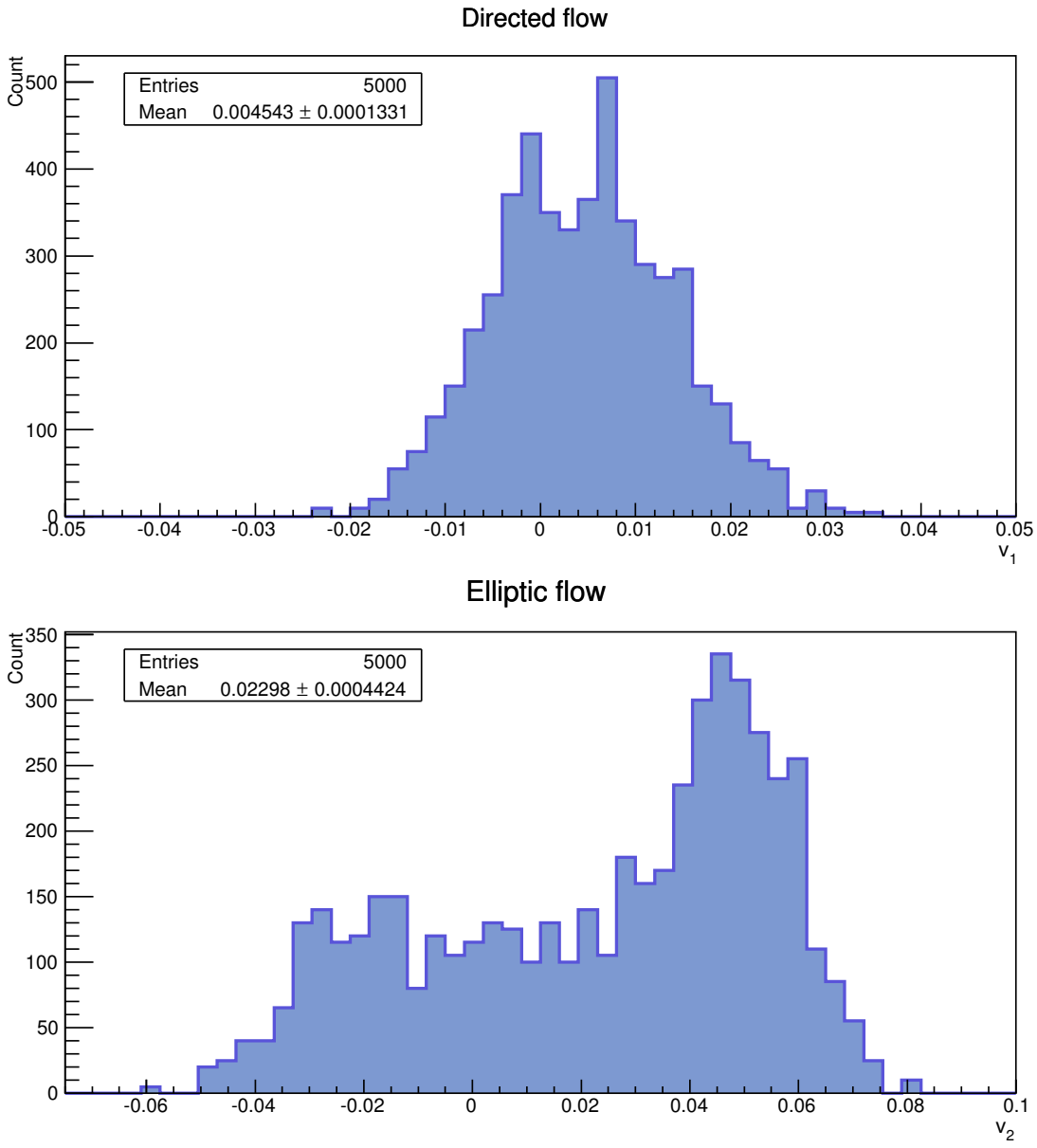

Figure 30: Event plane method method: v_1 and v_2 from 5000 events for pions.

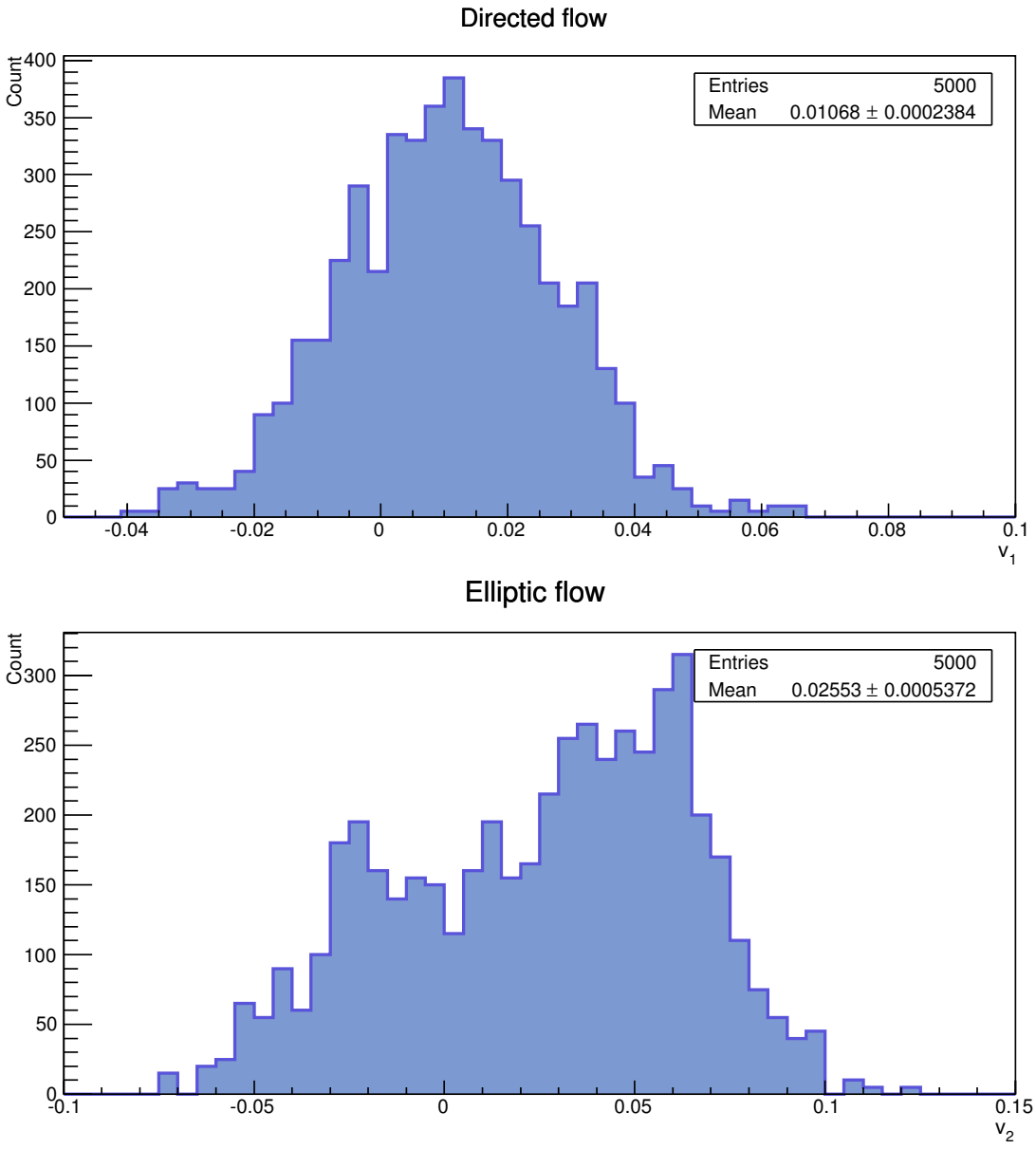

Figure 31: Event plane method method: v_1 and v_2 from 5000 events for kaons.

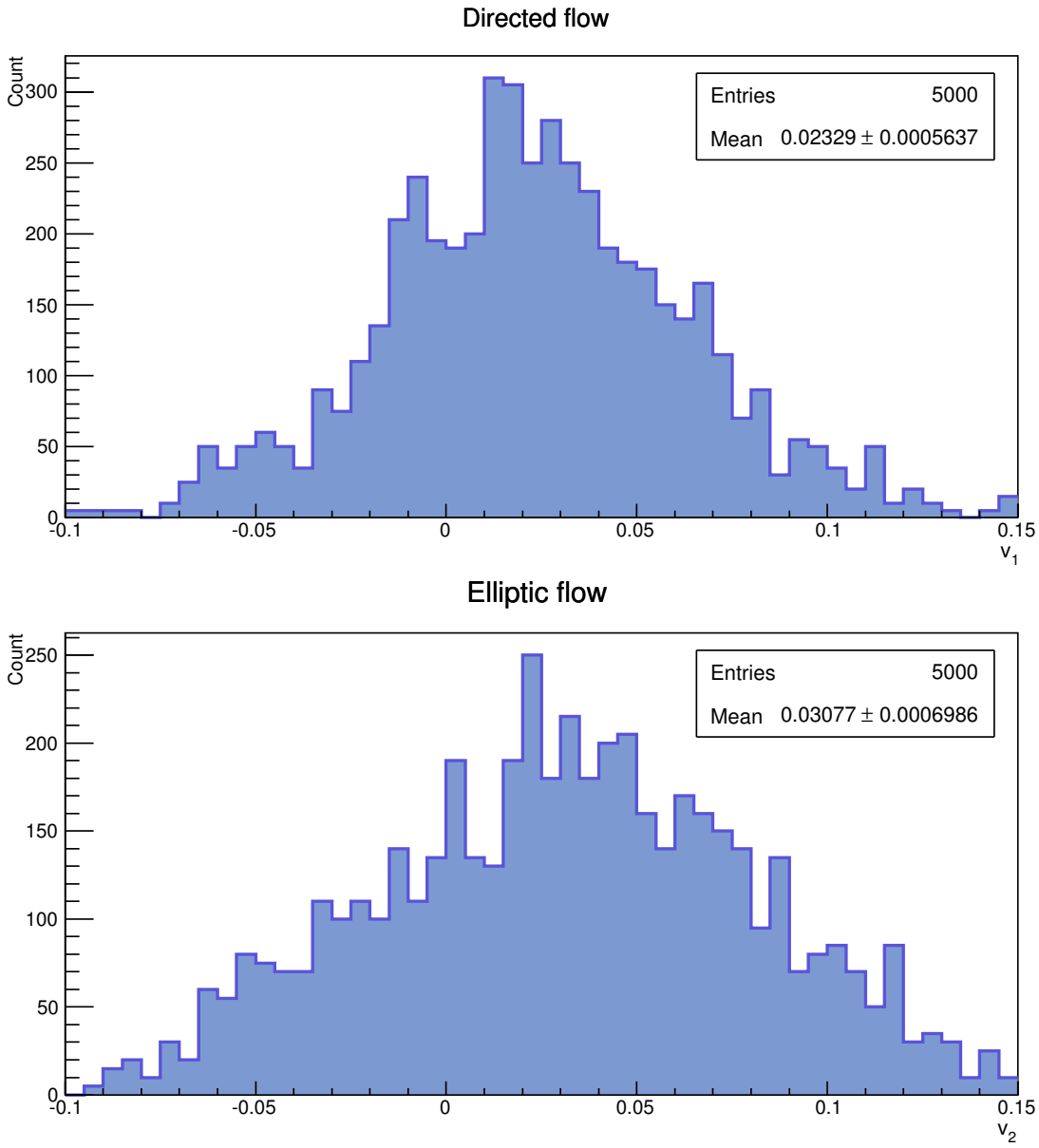

Figure 32: Event plane method method: v_1 and v_2 from 5000 events for protons.

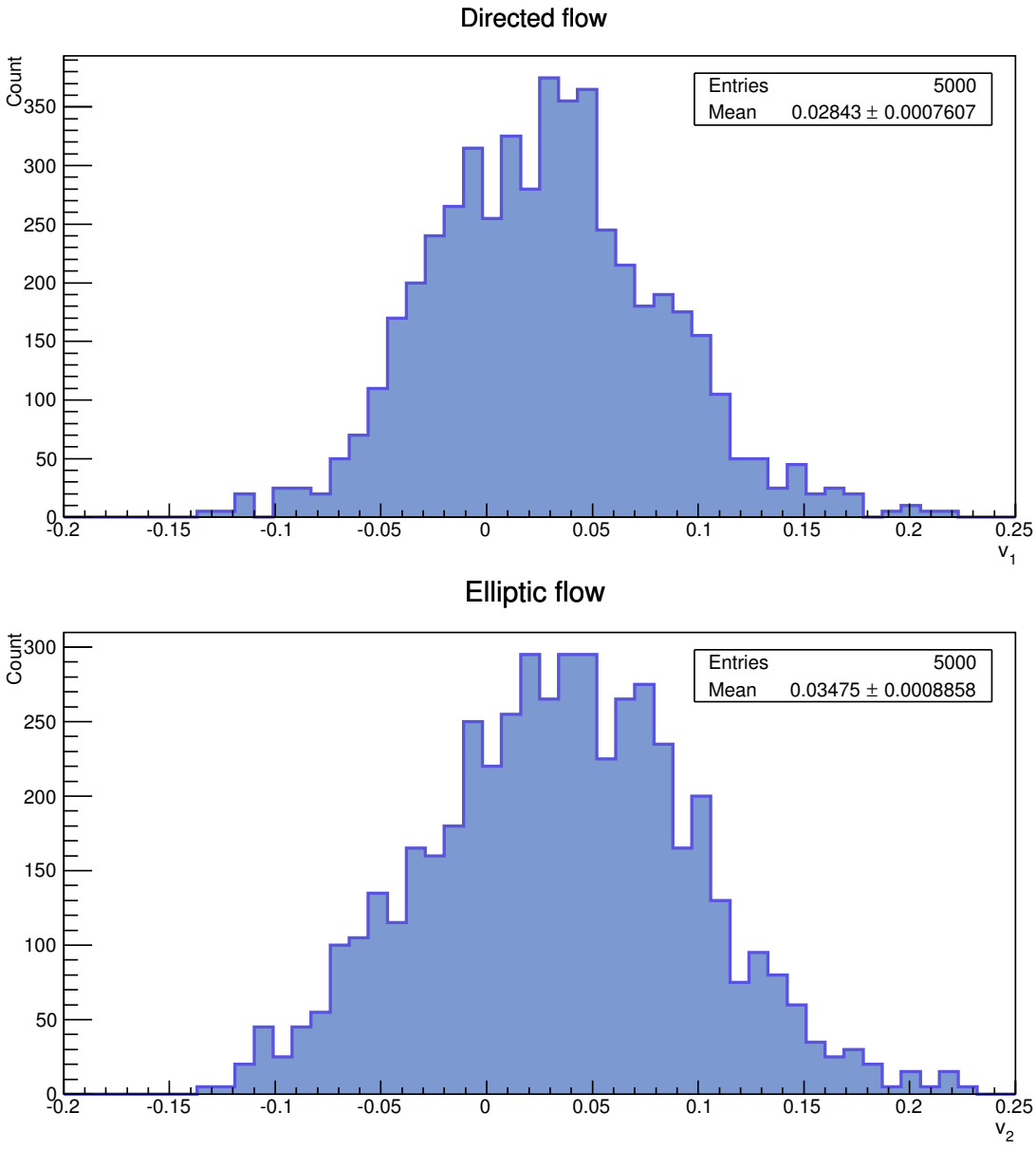

Figure 33: Event plane method method: v_1 and v_2 from 5000 events for Λ baryons.

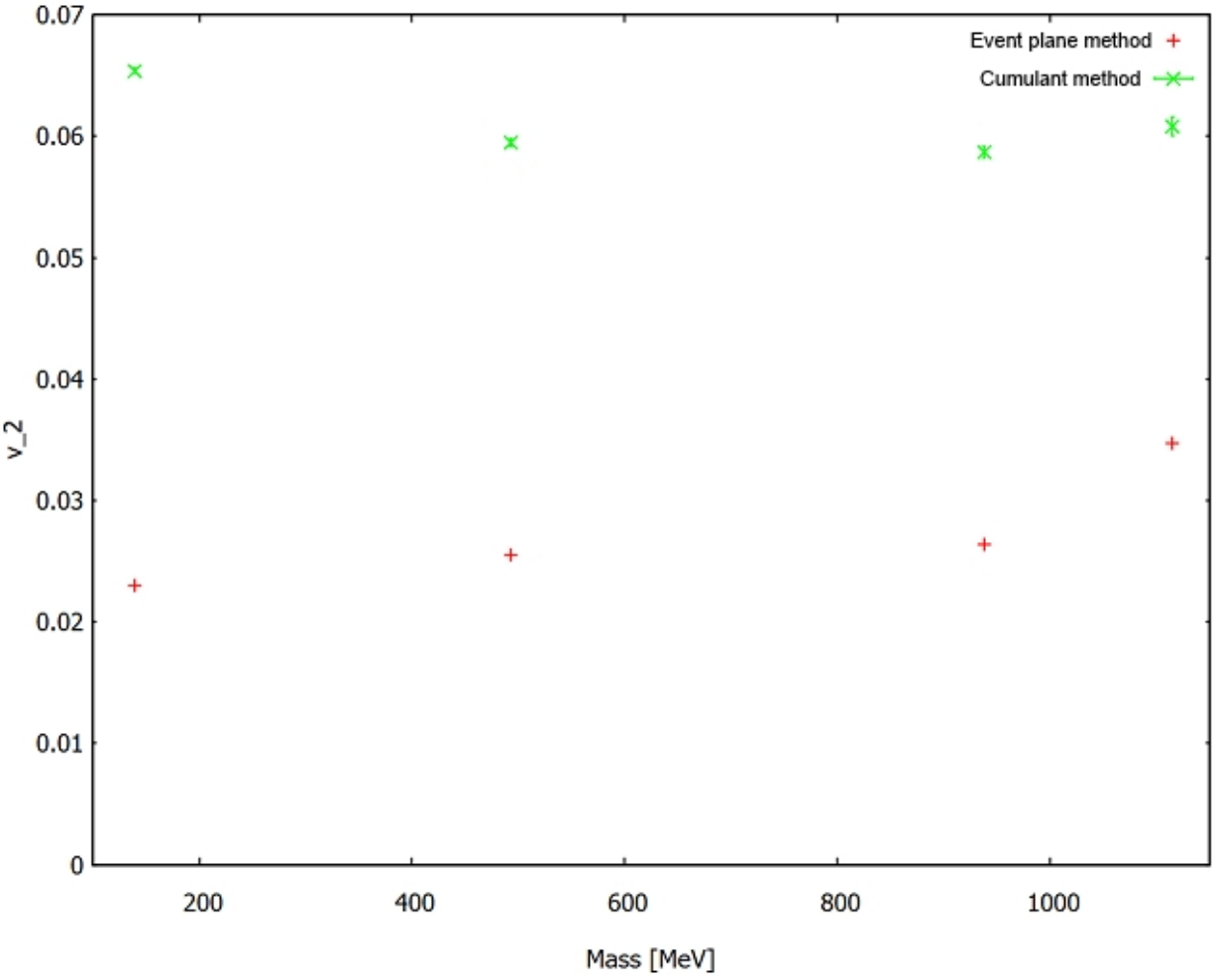

Figure 34: Event plane and cumulant method v_2 comparison.

Conlusion

In this thesis, we introduced quark-gluon plasma, discussed its hydrodynamical properties and the experimental evidence of its existence. We focused on collective flow, emphasizing the elliptic flow. We described several methods of computing flows and we discussed some of the difficulties one has to deal with during measuring and computing flows. We presented several of our own results obtained with the help of a toy Monte Carlo model. We introduced two methods of generating random numbers with desired distribution, compared it using the example of p_T and Φ distributions. Our analysis of the generated data agrees with the initial parameters. Moreover, we analyzed data produced by DRAGON [1] and discussed these results.

References

[1] TOMÁŠIK, Boris. DRAGON: Monte Carlo generator of particle production from a fragmented fireball in ultrarelativistic nuclear collisions. *Computer Physics Communications*, 180(9):1642 – 1653, 2009. http://www.sciencedirect.com/science/article/pii/S0010465509000745.

[2] McLERRAN, Larry and SAMIOS, Nicholas. *T.D. Lee: Relativistic heavy ion collisions and the Riken Brookhaven Center, BNL-77850-2007-CP*. Nov 2006. http://www.bnl.gov/isd/documents/35336.pdf.

[3] National Science Foundation, Columbia University. Nevis Laboratories, and Brookhaven National Laboratory. *Report of the Workshop on BEV/Nucleon Collisions of Heavy Ions - How and Why, November 29-December 1, 1974, Bear Mountain, New York, Supported by National Science Foundation and Nevis Laboratories, Columbia University*. Brookhaven National Laboratory, 1975. http://books.google.cz/books?id=fUgoMwEACAAJ.

[4] BRAUN-MUNZIGER, Peter. Chemical equilibration and the hadron-QGP phase transition. *Nuclear Physics A*, 681(1-4):119–123, 2001. 3rd Catania Relativistic Ion Studies. http://www.sciencedirect.com/science/article/pii/S0375947400004929.

[5] HEINZ, Ulrich and Raimond SNELLINGS. Collective flow and viscosity in relativistic heavy-ion collisions. *Annual Review of Nuclear and Particle Science*, 63(1):123–151, 2013. http://dx.doi.org/10.1146/annurev-nucl-102212-170540.

[6] GUÉNAULT, Tony. *Basic Superfluids*. Master's Series in Physics and Astronomy. Taylor & Francis, 2002. http://books.google.cz/books?id=zTRAicK9G64C.

[7] BASS, Steffen A. et. al. Microscopic models for ultrarelativistic heavy-ion collisions. *Progress in Particle and Nuclear Physics*, 41(0):255 – 369, 1998. http://www.sciencedirect.com/science/article/pii/S0146641098000581.

[8] LANDAU, Lev .D. and Evgeny M. LIFSCHITZ. *Course of Theoretical Physics*. Pergamon Press, 1987.

[9] BOER, Jan de. Introduction to the AdS/CFT correspondence, 2003. University of Amsterdam Institute for Theoretical Physics (ITFA) Technical Report 03-02, http://www-library.desy.de/preparch/desy/proc/proc02-02/Proceedings/pl.6/deboer_pr.pdf.

[10] GYULASSY, Miklos and Larry McLERRAN. New forms of QCD matter discovered at RHIC. *Nuclear Physics A*, 750(1):30 – 63, 2005. New Discoveries at RHIC: Case for the Strongly Interacting Quark - Gluon Plasma. Contributions from the RBRC Workshop held May 14-15, 2004. http://www.sciencedirect.com/science/article/pii/S0375947404011480.

[11] FLORKOWSKI, Wojciech. *Phenomenology of Ultra-Relativistic Heavy-Ion Collisions*. World Scientific, 2010. http://books.google.cz/books?id=4gIp05n9lz4C.

[12] Edward SHURYAK. Physics of strongly coupled quark-gluon plasma. *Progress in Particle and Nuclear Physics*, 62(1):48 – 101, 2009. http://arxiv.org/pdf/0807.3033v2.pdf.

[13] HEINZ, Ulrich and Maurice JACOB. Evidence for a New State of Matter: An Assessment of the Results from the CERN Lead Beam Programme. http://newstate-matter.web.cern.ch/newstate-matter/Science.html.

[14] ADAMS, J et al., STAR Collaboration. Evidence from d + Au measurements for final state suppression of high p_T hadrons in Au+Au collisions at RHIC. *Phys.Rev.Lett.*, 91:072304, 2003. http://arxiv.org/pdf/nucl-ex/0306024v3.pdf.

[15] BLAIZOT, Jean-Paul and François GELIS and Raju VENUGOPALAN. High energy pa collisions in the color glass condensate approach I: gluon production and the cronin effect. *Nuclear Physics A*, 743(1 - 3):13 – 56, 2004. http://www.sciencedirect.com/science/article/pii/S0375947404008139.

[16] VOLOSHIN, Sergei A. and Arthur M. POSKANZER and Raimond SNELLINGS. Collective phenomena in non-central nuclear collisions. *Relativistic Heavy Ion Physics*, 23:293–333, 2010. http://dx.doi.org/10.1007/978-3-642-01539-7_10.

[17] LUZUM, Matthew and Hannah PETERSEN. Initial state fluctuations and final state correlations in relativistic heavy-ion collisions. *Journal of Physics G: Nuclear and Particle Physics*, 41(6):063102, June 2014. http://stacks.iop.org/0954-3899/41/i=6/a=063102.

[18] ABELEV, B. et al., ALICE collaboration. Anisotropic flow of charged hadrons, pions and (anti-)protons measured at high transverse momentum in Pb-Pb collisions at $\sqrt{s_{NN}} = 2.76$ TeV. *Physics Letters B*, 719(1 - 3):18 – 28, 2013. http://www.sciencedirect.com/science/article/pii/S037026931300004X.

[19] AAMODT, K. et al., ALICE Collaboration. Higher harmonic anisotropic flow measurements of charged particles in Pb-Pb collisions at $\sqrt{s_{NN}}$=2.76 TeV. *Phys.Rev.Lett.*, 107:032301, 2011. http://arxiv.org/pdf/1105.3865v2.pdf.

[20] AAD, G. et al., ATLAS Collaboration. Measurement of the azimuthal anisotropy for charged particle production in $\sqrt{s_{NN}}$=2.76 TeV lead-lead collisions with the ATLAS detector. *Phys.Rev.*, C86:014907, 2012. http://arxiv.org/abs/1203.3087.

[21] CHATRCHYAN, S. et al., CMS Collaboration. Azimuthal anisotropy harmonics in ultra-central PbPb collisions at $\sqrt{s_{NN}} = 2.76$ TeV. Technical Report CMS-PAS-HIN-12-011, CERN, Geneva, 2014. http://arxiv.org/abs/1312.1845.

[22] BHALERAO, Rajeev S. and Jean-Yves OLLITRAULT and Subrata PAL. Event-plane correlators. *Phys. Rev. C 88*, 2013. http://arxiv.org/abs/1307.0980.

[23] PRESS, William H. and TEUKOLSKY, Saul A. and VETTERLING, William T. and FLANNERY, Brian P. *Numerical Recipes 3rd Edition: The Art of Scientific Computing*. Cambridge University Press, New York, NY, USA, 3 edition, 2007.

[24] ARGUIN J.-F. and GARREN, L. et. al. Monte Carlo particle numbering scheme. 2013. http://pdg.lbl.gov/2013/reviews/rpp2013-rev-monte-carlo-numbering.pdf.

[25] VEBERIĆ, Darko. Having Fun with Lambert W(x) Function. *ArXiv e-prints*, March 2010. http://arxiv.org/abs/1003.1628.